H$_2$O and CO$_2$ evolution in the Bandelier Tuff sequence reveals multiple and discrete magma replenishments

Clara M. Waelkens[1] · John Stix[1] · Erin Eves[1] · Carla Gonzalez[1] · David Martineau[1]

Abstract

The sequence of eruptions in the Bandelier magmatic system provides an opportunity to study volatile evolution through different stages of a large silicic magma chamber. The Lower Bandelier Tuff (LBT) and Upper Bandelier Tuff (UBT) eruptions offer a snapshot of a pre-eruptive magma chamber primed for eruption, while the sequence of Valle Toledo Member (VTM) eruptions open a window into the temporal evolution of the chamber's upper regions between the two super-eruptions. We measured H$_2$O and CO$_2$ concentrations in melt inclusions from the entire sequence of eruptions and identified three peaks in CO$_2$ concentrations: (1) in the middle of the LBT plinian airfall (increase in mean CO$_2$ concentrations from 27 ± 5 ppm at the base of the plinian to 173 ± 5 ppm in the mid-plinian); (2) in VTM group III (mean of 197 ± 5 ppm); and (3) in the middle of the UBT plinian airfall (mean of 54 ± 5 ppm at the base of the plinian to 101 ± 5 ppm in the mid-plinian). We propose that these increased CO$_2$ concentrations are due to injections of fresh magma into the system, whereby CO$_2$-rich vapours exsolved from the injected magma percolated through the magma chamber to increase CO$_2$ levels. Although the sharp increase in the LBT plinian indicates a rapid succession of recharge events in a short period of time, the gradually increasing CO$_2$ levels through the final VTM phase and the UBT plinian indicate that recharge events may have been spread over a longer period of time before the UBT eruption. Based on the theoretical and observed gradients in H$_2$O and CO$_2$ through the LBT and UBT sequence, we calculate a vapour phase equivalent to maximum 6.7 wt% of the magma body was exsolved from the LBT magma chamber; for the less degassed UBT, the exsolved vapour phase was maximum 4.2 wt% of the magma body. Our results indicate that the volatile composition of magmatic systems, with a particular focus on CO$_2$, can record evidence of magmatic recharge into the system and be an important tool in deciphering recharge events.

Keywords Melt inclusions · Volatiles · Silicic magma systems · Magmatic recharge · Supereruption

Introduction

Magmatic volatiles play a fundamental role in magma behaviour, both as dissolved species in the melt and in exsolved gas phases. They influence the behaviour of magma and can play a role in triggering volcanic eruptions. By studying the distributions of H$_2$O and CO$_2$ in a large silicic magma chamber, we can examine the pre-eruptive processes that take place in the chamber and how the chamber evolves towards

large-scale caldera-forming eruptions. We studied samples from Valles caldera, an archetype caldera system.

Geological setting

Often described as the type example of a resurgent caldera, Valles caldera is one of the three recently active resurgent caldera systems in the continental United States (Self et al. 1986). It is the youngest expression of the Jemez Mountains Volcanic Field (JMVF), a Miocene-Quaternary volcanic center in north-central New Mexico (Rowe et al. 2007) (Fig. 1). Located where the western edge of the 900-km-long, north–south Rio Grande Rift is intersected by the northeast-southwest trending Jemez volcanic lineament, the JMVF has produced the most voluminous and diverse volcanism in the region. Throughout its 13 million years of volcanic activity, it first erupted a basalt–rhyolite sequence, followed by two

✉ Clara M. Waelkens
  clara.waelkens@mail.mcgill.ca

[1] Department of Earth and Planetary Sciences, McGill University, Montreal, QC, Canada
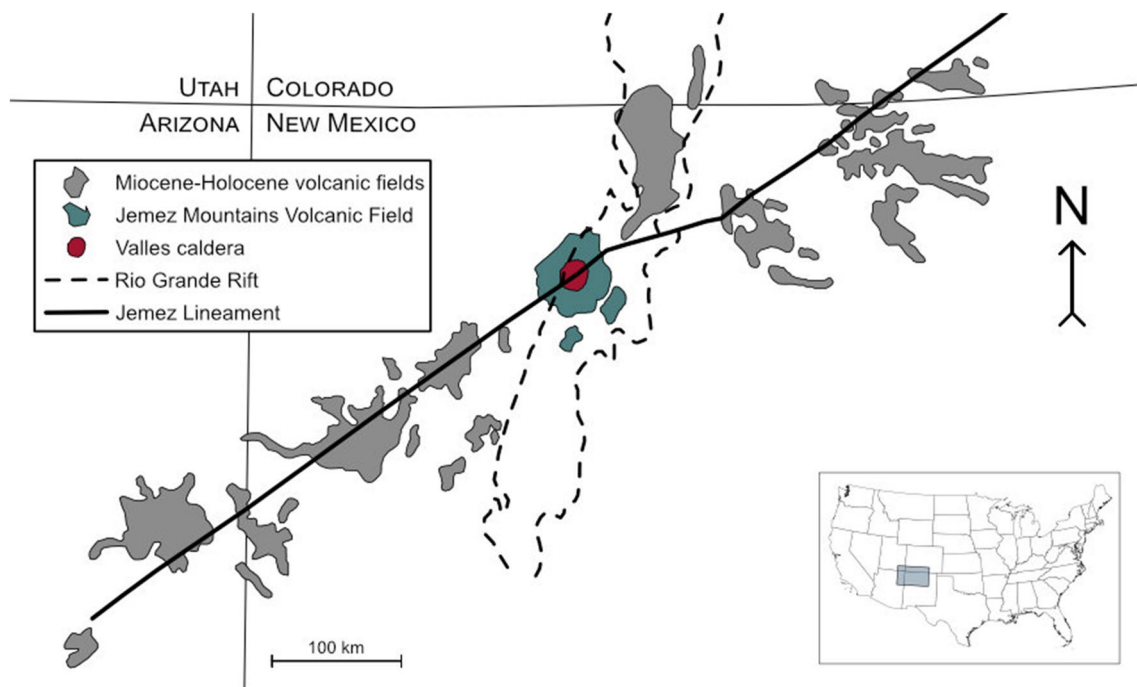
Fig. 1 Location of Valles caldera in the Jemez Mountains Volcanic Field, adapted from Goff and Gardner (2004)

basalt–andesite–rhyolite sequences, before culminating in the series of high-silica rhyolitic eruptions that formed Toledo and Valles calderas (Smith and Bailey 1968; Goff et al. 1989; Rowe et al. 2007). The Bandelier and related magmas represent an ideal system in which to study the role of volatiles in an evolving magma chamber. Its continuous sequence of eruptions permits us to examine the magma at different stages of differentiation, whereas the well-studied Bandelier system (e.g. Smith and Bailey 1968; Eichelberger and Koch 1979; Self et al. 1986; Gardner et al. 2010; Wilcock et al. 2013; Goff et al. 2014) allows us to use our conclusions regarding volatile evolution in a wider context. Although the evolution of H_2O concentrations has been studied in this system (Sommer 1977; Dunbar and Hervig 1992; Hervig and Dunbar 1992; Stix and Layne 1996), CO_2 has not. By considering H_2O and CO_2 together, we aim to obtain a full picture of the condition of magma storage, the nature of the exsolved vapour phase and the open-system processes that impacted the magmatic system throughout the sequence of eruptions. Given the fundamental role volatiles play in determining the behaviour of a magma, a good understanding of volatile behaviour is essential to decipher the workings of a magmatic system.

Eruptive history of Valles caldera

La Cueva member

The activity of the Valles–Toledo caldera system itself began with the 1.85 ± 0.07 Ma La Cueva Member of the Bandelier

Tuff, a unit of two distinct ignimbrites (Turbeville and Self 1988; Spell et al. 1990, 1996b). Referred to as the San Diego Canyon Ignimbrites in older literature, these lithic-rich pyroclastic rocks contain pumices that are both petrographically and geochemically similar to the least-evolved material in the later-erupted Lower Bandelier Tuff. Hence the La Cueva ignimbrites are suggested to be the result of an early tapping of the Bandelier magmatic reservoir, before further fractionation produced the more evolved Lower Bandelier Tuff (Spell et al. 1990). With a maximum total thickness of 85 m and an estimated volume of less than 20 km^3 dense-rock equivalent (DRE), the La Cueva Member is by far the smallest of the Bandelier phases (Spell et al. 1996b; Wolff and Ramos 2014). The vents were centred to the southwest of what is now Valles Caldera, where the eruption may have led to collapse and the formation of one or more calderas, which were later overprinted during the larger Lower and Upper Bandelier Tuff eruptions (Spell et al. 1990; Gardner et al. 2010).

Lower Bandelier Tuff

The La Cueva Member was soon followed by the first cataclysmic eruption, which at 1.608 ± 0.010 Ma deposited the Lower Bandelier Tuff (LBT) (Spell et al., 1996b). An estimated 400–500 km^3 DRE of magma (minimum 216 km^3, maximum 550 km^3) (Cook et al., 2016) was erupted, first in a plinian phase which deposited the Guaje Pumice Bed, followed by the voluminous Otowi ignimbrite (Fig. 2). The
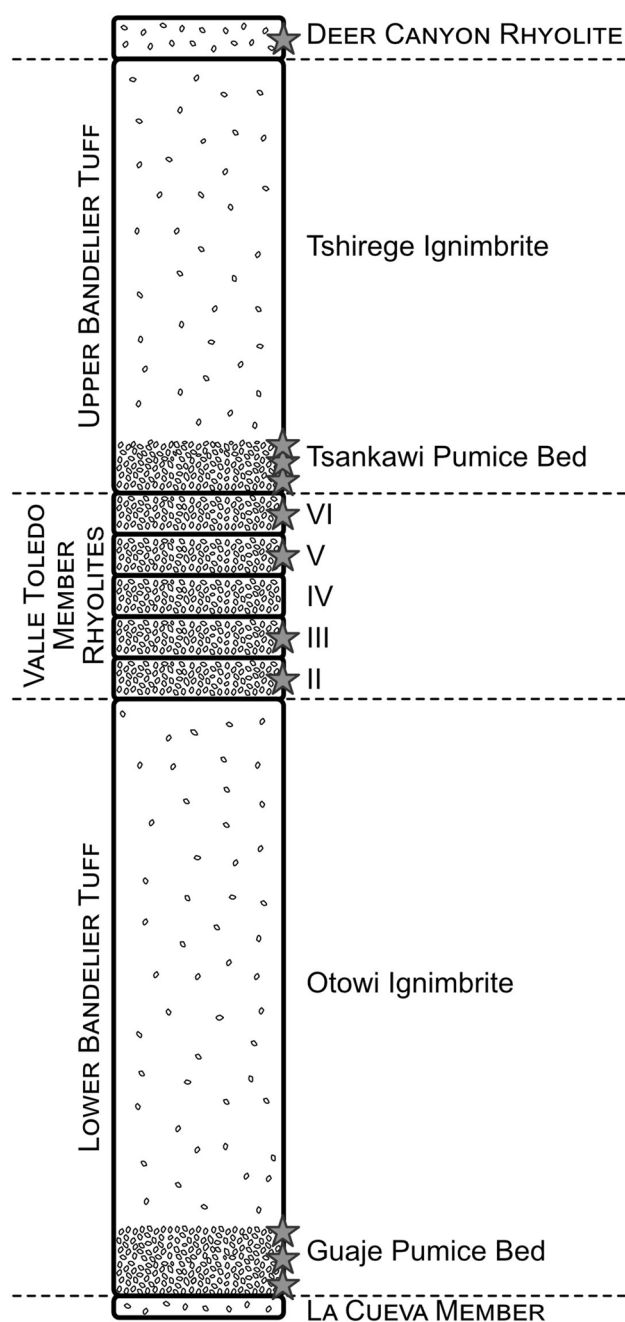
Fig. 2 Simplified stratigraphic column of the sequence of eruptions. The VTM and Deer Canyon Rhyolite units are not to scale. The plinian and ignimbrite phases are indicated for each of the two Bandelier eruptions. The VTM is simplified and displays more variety in outcrop than is represented here. Stars represent the stratigraphic horizons that were analysed in this study

eruption was initiated from centrally located vents, but as the eruption advanced and the magma chamber roof failed, the eruption shifted to multiple ring fault vents in the southwestern part of what is now Valles Caldera (Self et al. 1986). Widespread collapse formed Toledo caldera

(Spell et al. 1990, 1996b). The plinian phase erupted an estimated 65 km^3 DRE (Cook et al., 2016) and is far smaller than the ignimbrite. Five fall units were defined (A–E), with different dispersal directions (Self et al. 1986). The ignimbrite outside the caldera is largely nonwelded and represents a single cooling unit. Maximum preserved thicknesses inside the caldera reach 830 m and outside the caldera up to 120 m (Kuentz 1986; Broxton et al. 1995; Brundstad 2013). The LBT consists almost entirely of high-silica rhyolite with similar major element composition, but varying minor and trace element composition. Variations in composition among individual pumices indicate a compositionally heterogeneous and possibly zoned magma chamber (Kuentz 1986; Dunbar and Hervig 1992), while Sr and Pb isotopes indicate zonation consistent with successive pulses of rejuvenation and melting of a crystal mush (Wolff and Ramos 2014; Wolff et al. 2015).

Valle Toledo Member rhyolites

As the eruption ended, erosional processes started to act on the newly-formed caldera walls, producing vast quantities of sediment. At the same time, renewed volcanic activity within the caldera produced rhyolitic domes and tephra deposits, part of which are preserved on caldera rims and interbedded with the sedimentary material in canyons outside the caldera. The volcanic deposits and sediments are grouped together into the Cerro Toledo Formation, with the volcanic units making up the Valle Toledo Member (VTM) (previously referred to as the Cerro Toledo Rhyolites; Gardner et al. 2010). The volcanic activity spans the entire 360 ky interval between the two major Bandelier eruptions (Spell et al. 1996b) and is interpreted as periodic tapping of an evolving magma related to the Bandelier Tuffs, allowing an exceptional and unique window into the evolution and reestablishment of the magma chamber.

The VTM was first described by Griggs (1964) and mapped by Smith et al. (1970) and has since been the focus of several volcanological, geochemical and geochronological studies (Heiken et al. 1986; Stix et al. 1988; Stix 1989; Stix and Gorton 1993, 1990a, 1990b; Broxton et al. 1995; Stix and Layne 1996; Spell et al. 1996a, 1996b; Jacobs and Kelley 2007; Slate et al. 2007; Campbell et al. 2009). The rhyolitic tephras are exposed in several sections, which were described by Stix (1989). Based on the trace elements, the VTM rhyolites were divided into five geochemical groups, groups II–VI, which can be recognised across the different sections (Stix and Gorton 1990a, 1990b, 1993). Group II, the first erupted VTM rhyolites, has been shown to be comagmatic with the LBT ignimbrite, representing a final pulse from the emptied LBT magmatic system (Stix and Gorton 1993). Subsequently,

group III (1.536 ± 0.018 Ma; Spell et al. (1996b)) exhibits signs of intrusion of fresh magma and heralds a new evolutionary phase of the UBT magmatic system. Trace elements indicate the rhyolites erupted in the subsequent phases (IV to VI) are the result of different stages of differentiation of the same melt (Stix and Gorton 1993; Stix and Layne 1996).

Upper Bandelier Tuff

The second cataclysmic eruption, depositing the Upper Bandelier Tuff (UBT), occurred at 1.256 ± 0.010 Ma (Phillips et al. 2007) and formed a second caldera, Valles caldera, which overprinted the earlier Toledo caldera. With a total volume of 400 km^3 DRE (best estimate; Goff 2010; Goff et al. 2011, 2014), the UBT represents a slightly smaller eruption than the LBT. The present caldera has a diameter of 19–24 km, with the caldera wall rising from a few tens of meters to 600 m above the caldera floor (Smith and Bailey 1968). The eruption started from a central vent near the location of the central LBT vents. Evidence for later transition to a ring-fracture vent is not conclusive, but most ignimbrite subunits are interpreted as having been erupted from a vent on the eastern side of the caldera (Self et al. 1986; Warren et al. 2007). Similar to the LBT, this eruption also began with a plinian phase, which formed the Tsankawi Pumice Bed, followed by the Tshirege ignimbrite. Six units with different dispersals have been defined in the Tsankawi (A–F), four coarser pumice units and two finer ash fall units (Self et al. 1986). The ignimbrite is made up of at least four different cooling units (Broxton et al. 1995; Brundstad 2013) and is variably welded. Maximum intracaldera thicknesses are 1150 m, while outside the caldera thicknesses reach 270 m (Nielson and Hulen, 1984). The UBT comprises mostly high- to low-silica rhyolite, with approximately 1% hornblende dacite pumices concentrated in the Tsankawi Pumice Bed and early-erupted ignimbrite, as well as rare syenitic crystal clots in the later-erupted deposits (Caress 1996; Stimac 1996; Wilcock et al. 2013). Although the Tshirege ignimbrite is generally considered a normally zoned ignimbrite, evidence points towards limited reverse zoning in the upper part of the ignimbrite (Goff et al. 2014).

Valles rhyolite

Volcanic activity continued after eruption of the UBT and lasted until 0.34 Ma (Goff et al. 2011). All deposits erupted after the UBT are grouped in the Valles Rhyolite. Resurgence occurred rapidly, beginning soon after the eruption of the UBT and collapse of Valles caldera (Phillips et al. 2007). The Deer Canyon Rhyolite is considered to represent residual magma remaining from the UBT eruption, while the Redondo Creek Rhyolite appears to reflect a new influx

of silicic magma (Spell et al. 1990; Kennedy et al. 2012; Wilcock et al. 2013). The resurgent dome, Redondo Peak, rose 1000 m above the caldera floor, driven by the injection of hotter, more primitive magma into the residual magma chamber (Smith and Bailey 1968; Goff et al. 2011; Kennedy et al. 2012). The Deer Canyon Rhyolite (1.229–1.238 Ma) and Redondo Creek Rhyodacite (1.208–1.239 Ma) were erupted during resurgence (Phillips et al. 2007). Resurgence was followed by the extrusion of a series of rhyolitic lava dome complexes, lava flows and tephras along the ring fracture system (1.22–0.52 Ma) (Wolff and Gardner 1995; Gardner et al. 2010). The East Fork Member represents the most recent volcanic activity in Valles caldera, erupting a series of rhyolitic lavas and tephras between 60 and 34 ka (Gardner et al. 2010; Goff et al. 2011). While this may represent the end of post-caldera activity, it has also been suggested that this activity may indicate the start of a new cycle of activity in Valles Caldera (Wolff and Gardner 1995).

Methodology

Sample collection

We sampled the plinian phases of both the LBT and the UBT and the different pyroclastic horizons of the Valle Toledo Member rhyolites (sample locations listed in Table A2 in supplementary information). The Guaje Pumice Bed (the LBT plinian airfall) was sampled east of the caldera, where it is thickest. Samples from the middle of the plinian phase and the transition to the ignimbrite were collected in the Copar Pumice Mine, along Guaje Canyon. While the base of the plinian phase is not exposed in the Copar mine, all five plinian fall units are preserved. Unit A is most extensive and forms a massive, ~ 6-m-thick deposit with little variation, followed by units B to E that together form a bedded ~ 1.5-m-thick section underlying the ignimbrite. We sampled the upper units to represent the top of the plinian phase (fall unit E) and the top of the massive unit A to represent the middle of the plinian phase. The base of the plinian was sampled in a roadside outcrop along highway 502, where the unconformity with the Cerros del Rio basalt is well exposed (Fig. 3). Owing to different prevailing wind directions during eruption, the Tsankawi Pumice Bed is most extensive west of the caldera. We collected samples representing the base, middle and top of the plinian airfall at a roadside outcrop along country road 257. All three samples were taken from fall unit B as defined by Self et al. (1986), which is the most extensive and dominant fall unit of the UBT plinian sequence (Fig. 3).

For the VTM rhyolites, we sampled each geochemical group as defined by Stix (1989) and Stix and Gorton (1990a) in the pyroclastic VTM deposits. We collected
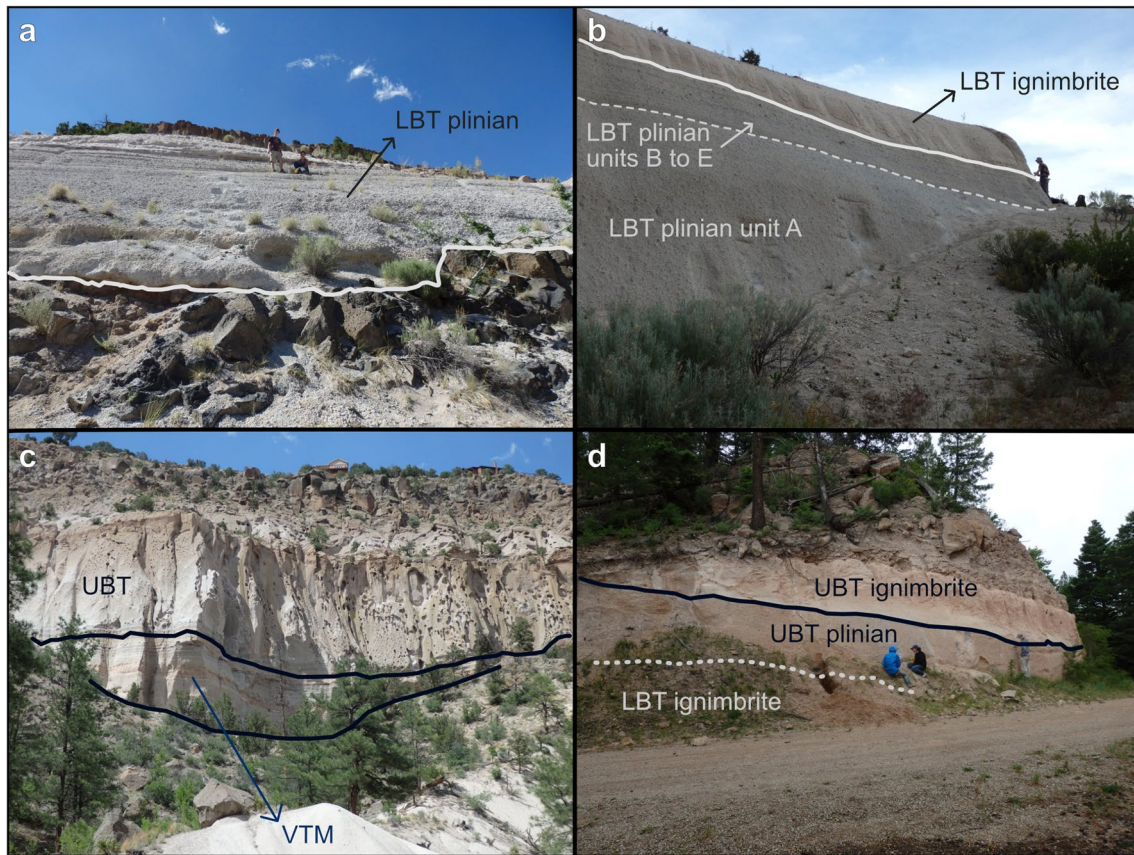
Fig. 3 Outcrops of the LBT, UBT and VTM rhyolites. **a** The base of the LBT plinian, exposed along highway 502. The unconformity with the underlying Cerros del Rio basalt is drawn. **b** Outcropping of the top of the LBT plinian unit and the base of the overlying ignimbrite at the Copar Pumice Mine. The massive unit A and smaller, bedded units B to E of the plinian airfall phase are indicated. **c** Example of an outcrop of the VTM rhyolites in Pueblo Canyon, to the east of Los Alamos. This is section 15 as described by Stix (1989). The VTM and overlying UBT are labelled on the photograph. Houses on the canyon edge for scale. **d** UBT plinian phase and overlying ignimbrite in a roadside outcrop along country road 257, west of the caldera. The approximate base of the plinian airfall and boundary with the LBT ignimbrite is drawn, as the boundary is hidden under soil

samples from three outcrops where the pyroclastic VTM is exposed: as described by Stix (1989). Within these outcrops, we sampled stratigraphic units 7–3, 15–9, 6–2, 15–11 and 6–8, using sample locations and outcrops descriptions from Stix (1989). These units were defined by Stix and Gorton (1990a) to be part of, respectively, geochemical groups II to VI. The Deer Canyon Rhyolite had been sampled previously by Wilcock (2010) and Wilcock et al. (2013). We did not collect new samples, but used pumices from the tephra units of the Deer Canyon Rhyolite that had been collected for these past studies.

The LBT and the UBT plinian phases have the highest crystal contents of our sample set and have 10–20% phenocrysts. Quartz and sanidine dominate, with less than 5% of more mafic phenocrysts including Fe–Ti oxides, pyroxene, hornblende as well as zircon (Kuentz 1986; Balsley 1988) The VTM rhyolites are poorer in crystals than the Bandelier magmas (<5% phenocrysts), but phenocrysts are similarly mostly quartz and sanidine, with trace amounts of plagioclase, Fe–Ti oxides and pyroxene (Stix and Layne, 1996). Within the Deer Canyon Rhyolite, crystal content varies locally from aphyric to crystal-rich, but phenocrysts are still dominated by quartz and sanidine (Goff et al., 2011).

Sample preparation

In samples where pumices were sufficiently large (approximately > 5 cm), the pumices were processed individually. In samples where pumice clasts were smaller and which were sampled in bulk, we selected the largest clasts and processed these in bulk. To select melt inclusion-bearing crystals, the pumices were lightly crushed and sieved. We handpicked individual quartz and sanidine crystals from the − 0.5 to 0.5 φ fraction (0.71–1.4 mm), as it contained complete, undamaged crystals. Crystals selected contained large, clear
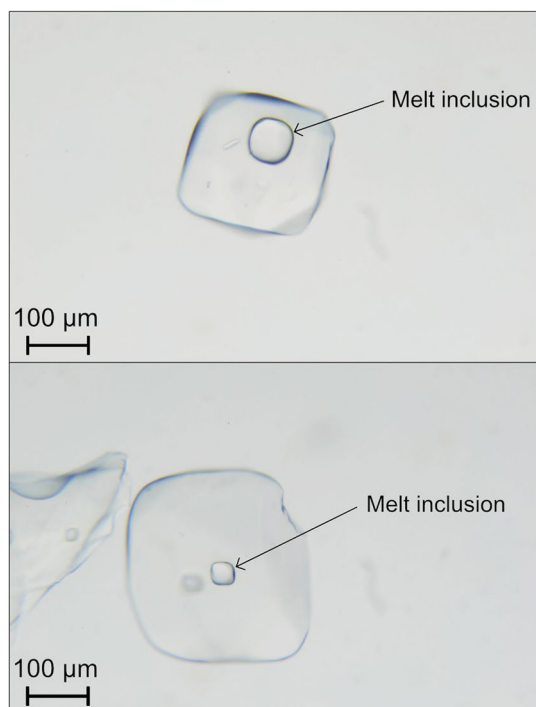
melt inclusions free of bubbles and crystals and without evidence of leakage or breakage (Fig. 4). The majority of melt inclusion-hosting crystals were quartz, with a smaller proportion of sanidine. The majority of sanidine crystals broke during polishing and became unusable, so that the analysed melt inclusions were principally hosted in quartz. We only analysed melt inclusions that comprised 100% fresh glass. If a melt inclusion contained a bubble or the host crystal had a crack at or near the melt inclusion, that inclusion was not analysed. The individual crystals were ground and polished to expose the melt inclusions on both sides for transmission Fourier-transform infrared spectroscopy (FTIR).

FTIR analysis

Analytical conditions

H_2O and CO_2 were measured by transmission FTIR with a Bruker Tensor 27 infrared spectrometer and a Bruker Hyperion 2000 microscope. The entire instrument was placed in a protective plastic shroud that was purged with ultra-high purity N_2 gas, to allow for detection of low CO_2 concentrations without influence of atmospheric CO_2. The ambient CO_2 in the shroud was monitored with a PP Systems SBA-5 CO_2 gas analyzer and kept below 20 ppm CO_2.

The polished wafers were placed on a NaCl salt plate for analysis and measured with a 15X objective IR lens.

Fig. 4 Examples of melt inclusion in the base of the LBT plinian. The analysed melt inclusions were all free of bubbles or crystals

Spectral resolution was 4 cm^{-1} for all melt inclusions and 512 scans were made for each spectrum. We used optical apertures between 40 and 100 μm, adapting the aperture for each melt inclusion in order to maximize the aperture and thereby reduce analytical noise.

Absorbance peak heights were measured at 5200 cm^{-1} (H_2O_m), 4500 cm^{-1} (OH$^-$) and 3450 cm^{-1} (H2O$_t$) according to Newman et al. (1986). Owing to the high water contents, the H$_2$O$_t$ peak at 3450 cm^{-1} was saturated with a flat top for the majority of the analyses and was therefore not usable. The total water contents were calculated following the rhyolite glass calibration of Zhang et al. (1997), which takes into account the variation of the extinction coefficients for H_2O_m and OH$^-$ with total water content. H$_2$O$_{total}$ is calculated as the sum of the H_2O_m and OH$^-$ contributions:

$$C_{H_2O_m} = a_0 * \overline{A}_{5200} / (\rho / \rho_0)$$

$$C_{OH^-} = \overline{A}_{4500} * \left(b_0 + b_1 * \overline{A}_{5200} + b_2 * \overline{A}_{4500}\right) / (\rho / \rho_0)$$

where a_0, b_0, a_1 and b_1 are fitting parameters, with $a_0 = 0.04217$ mm, $b_0 = 0.04024$ mm, $b_1 = -0.02011$ mm^2, $b_2 = 0.0522$ mm^2, C$_{H2Om}$ and C$_{OH^-}$ are, respectively, the concentrations of molecular H_2O and of H_2O present as OH$^-$, $\bar{A}_{5200}$ and $\bar{A}_{4500}$ are, respectively, the peak heights of the H$_2$O$_m$ and OH$^-$ peaks divided by the sample thickness and ρ / ρ_0 is the density ratio of hydrous to anhydrous glass. Sample thickness is not explicitly defined in the formula, but it is accounted for in the normalised peak heights $\bar{A}_{5200}$ and $\bar{A}_{4500}$.

For CO_2 we measured the absorbance peak height at 2350 cm^{-1} and calculated concentrations using the Beer–Lambert law (Newman et al., 1986, 1988):

$$C_{CO_2} = M_{CO_2} * A_{2350} / (\rho * d * \varepsilon_{2350}) * 10^6$$

where C$_{CO2}$ is the concentration of CO_2 (ppm), M$_{CO2}$ the molar mass of CO_2 (g/mol), A$_{2350}$ the absorbance for the CO_2 peak at 2350 cm^{-1}, ρ the density of the glass (g/L), d the thickness of the wafer (cm) and ε the extinction coefficient for the CO_2 peak (L mol^{-1} cm^{-1}). This coefficient for rhyolite glasses is 1214 L mol^{-1} cm^{-1} (Behrens et al. 2004).

The thickness of the samples was measured using the FTIR stage, which was calibrated against a digital micrometer and has been shown to yield good agreement with the interference fringe method for measuring thicknesses (Lucic et al. 2016). The density of the glasses was calculated using the formula of R. Lange, as described in Luhr (2001) (Table A2 in supplementary information), based on the published major element compositions of melt inclusions in the LBT (Dunbar and Hervig 1992), the UBT and the VTM rhyolites (Stix and Layne 1996).

Errors on FTIR data

The two principal sources of error in the determination of H_2O and CO_2 concentrations are wafer thickness and measurement of absorbance. The inherent error based on the choice of extinction coefficients was reduced by the use of the calibration of Zhang et al. (1997), which accounts for the variability of extinction coefficients for H_2O_m and OH^-. The uncertainty on wafer thickness was minimized through repeated thickness measurements and reduced to < 5 μm. Subjectivity in measuring absorbance peak heights was minimised by measuring each melt inclusion 3–5 times and by re-analysing several melt inclusions on different days. To monitor the consistency of our results and test the correct functioning of the instrument, we analysed a rhyolitic standard glass, M6N (Westrich and Gerlach 1992, Devine et al. 1995), at the beginning and end of each analysis session. M6N contains 5.1 wt% H_2O (Westrich and Gerlach 1992; Thomas 2000) and 170 ppm CO_2 (unpublished value, lab estimate).

Each melt inclusion was analysed several times in the same analytical session and repeat analyses on different days were done for certain melt inclusions to test the reproducibility of the results. The consistency of our results varies with inclusion size: the smaller the melt inclusions, the smaller the aperture diameter and the noisier the spectra, which increases the error on the absorbance. For the majority of our melt inclusions, repeat analyses yielded reproducibility of ± 2 ppm for CO_2 and of ± 0.1 wt% for H_2O, although smaller melt inclusions (wafer thickness < 45 μm) yielded

errors of ± 5 ppm CO_2 and ± 0.2 wt% (detailed results per analysis in supplementary information). Based on the silicic standard glasses [M6N, M3N and PCD from Devine et al. (1995)] practical detection limits of ~ 10 ppm CO_2 and 0.1 wt% H_2O were determined for the method.

Results

Lower Bandelier Tuff

Melt inclusions are abundant in the LBT. They consist of clear glass and are frequently up to 150–200 μm in diameter. We analysed 33 melt inclusions from three different samples from the LBT plinian phase: one from the base of the unit, representing the earliest LBT plinian (10 melt inclusions), one from the top of the plinian phase at the transition to the ignimbrite (13 melt inclusions) and one sampled just below the bedded part of the plinian phase, taken to represent mid-plinian conditions (10 melt inclusions).

As shown in Fig. 5, the H_2O contents of the LBT inclusions show very similar averages and ranges. The dissolved CO_2 contents tell a different story. The earliest plinian melt inclusions contain very little CO_2, but CO_2 increases sharply at the mid-plinian. The top of the plinian airfall also has higher CO_2 and also exhibits the widest range of values. Looking at the mean CO_2 concentration for each sample, we see a sixfold increase, from 27 ppm at the base of the plinian to 173 ppm in the mid-plinian,
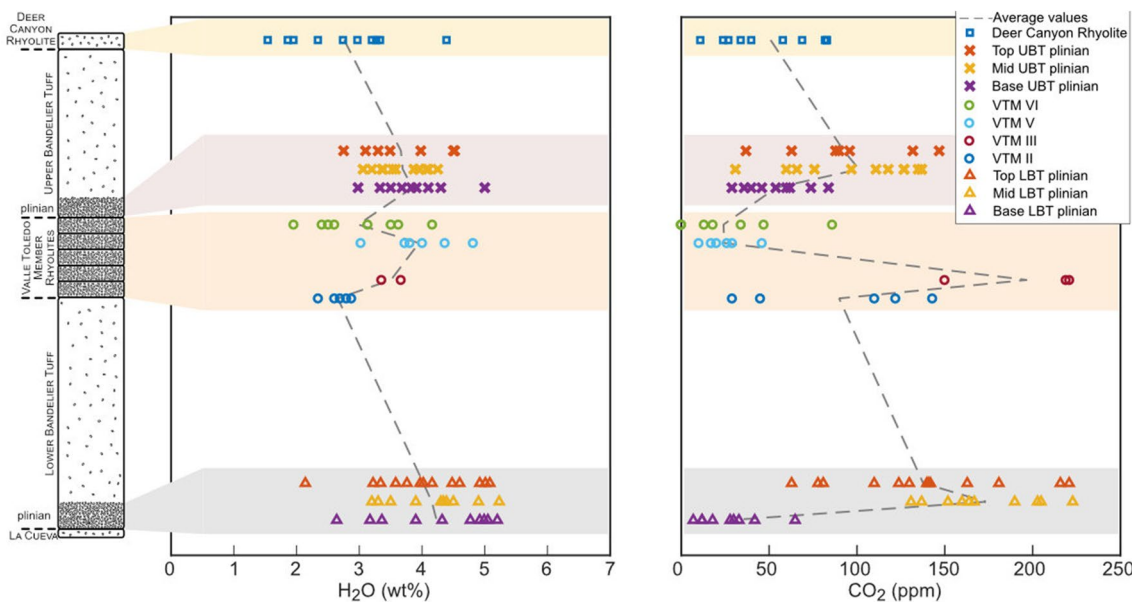
Fig. 5 Overview of H_2O and CO_2 concentrations, plotted as a function of stratigraphy. Average concentrations per unit are plotted as a dashed line. Stratigraphic column as in Fig. 2

Table 1 Summary of the H_2O and CO_2 data, with for each sample whether it was a bulk sample (B) or consisted of individual pumices (IP); host material is listed for each melt inclusion and is predominantly quartz (Q) with a few sanidines (San)

Formation and unit		Melt inclusion ID	Host material	H_2O (wt%)	CO_2 (ppm)
Deer Canyon Rhyolite (IP)		08-07_9	Q	2.7	40
		08-07_29	Q	1.5	24
		08-07_33	Q	2.0	27
		08-07_46	Q	3.2	83
		08-07_55	Q	1.9	11
		08-07_59	Q	3.3	69
		08-07_65	Q	4.4	83
		08-07_72	Q	3.0	82
		08-07_83	Q	2.3	34
		08-07_84	Q	3.3	58
Upper Bandelier Tuff plinian airfall	Top UBT plinian (B)	VC16-33_7_MI I	Q	4.0	37
		VC16-33_7_MI II	Q	4.5	132
		VC16-33_11	Q	4.5	147
		VC16-33_15_MI I	Q	3.1	88
		VC16-33_17	Q	3.5	96
		VC16-33_20_MI I	Q	2.8	90
		VC16-33_22	Q	3.3	63
	Middle UBT plinian (B)	VC16-30_1	Q	3.4	127
		VC16-30_2	Q	4.0	76
		VC16-30_3	Q	4.1	111
		VC16-30_4_MI1	Q	3.5	97
		VC16-30_4_MI2	Q	3.2	31
		VC16-30_6	Q	3.6	66
		VC16-30_8	Q	4.1	118
		VC16-30_9a	San	4.3	135
		VC16-30_12	Q	3.4	137
		VC16-30_13	Q	3.9	127
		VC16-30_14	Q	3.1	60
		VC16-30_15	Q	4.0	137
	Base UBT plinian (B)	VC16-28_3A	Q	3.9	84
		VC16-28_4	Q	3.8	74
		VC16-28_5	Q	4.3	46
		VC16-28_6	Q	3.5	29
		VC16-28_7	Q	5.0	60
		VC16-28_8	Q	3.0	36
		VC16-28_11	Q	4.1	54
		VC16-28_18	Q	3.7	62
		VC16-28_19	Q	3.3	40
		VC16-54(1)_1	Q	3.6	34

Table 1 (continued)

Formation and unit		Melt inclusion ID	Host material	H_2O (wt%)	CO_2 (ppm)
	VTM group VI (IP)	VC16-54(1)_2	Q	2.6	< dl
		VC16-54(1)_4	Q	4.2	< dl
		VC16-54(1)_5	San	2.4	13
Valle Toledo Member rhyolites		VC16-54(1)_6a	San	3.1	< dl
		VC16-54(1)_7	San	2.5	47
		VC16-54(1)_12	Q	2.0	86
		VC16-54(1)_13	Q	3.5	18
	VTM group V (B)	VC16-37_2	San	4.8	20
		VC16-37_4a	San	3.0	46
		VC16-37_6	Q	3.8	17
		VC16-37_7	Q	3.7	26
		VC16-37_9	Q	4.0	29
		VC16-37_17	Q	4.4	10
	VTM group III (IP)	VC16-40_3	San	N/A	219
		VC16-40_6	Q	3.7	221
		VC16-40_8a	San	3.4	150
	VTM group II (B)	VC16-20_1a	San	2.9	110
		VC16-20_2	Q	2.7	45
		VC16-20_3	Q	2.8	143
		VC16-20_5	Q	2.3	122
		VC16-20_8	Q	2.6	29
Lower Bandelier Tuff plinian airfall	Top LBT plinian (IP)	VC16-03a_2	Q	4.2	141
		VC16-03a_8	Q	2.1	78
		VC16-03a_10	Q	5.1	216
		VC16-03b_11	Q	4.9	110
		VC16-04b_31	Q	4.0	142
		VC16-04b_32	San	4.5	124
		VC16-04b_34	Q	5.0	81
		VC16-04c_42	Q	3.8	140
		VC16-04c_44	Q	3.2	221
		VC16-04c_45	Q	4.6	163
		VC16-04c_47	Q	3.3	63
		VC16-04c_48	Q	4.0	181
		VC16-04c_50	Q	3.6	130
	Middle LBT plinian (B)	VC16-09_1_MI1	Q	4.5	167
		VC16-09_1_MI2	Q	3.2	137
		VC16-09_2	Q	4.9	190
		VC16-09_4	Q	4.3	223
		VC16-09_5	Q	3.9	203

Table 1 (continued)

Formation and unit	Melt inclusion ID	Host material	H$_2$O (wt%)	CO$_2$ (ppm)
	VC16-09_6	Q	3.5	164
	VC16-09_8	Q	5.2	205
	VC16-09_10	Q	3.3	152
	VC16-09_13a	Q	4.4	131
	VC16-09_14	Q	4.3	160
	VC16-48A_03A	San	2.6	18
	VC16-48A_06	Q	3.2	12
Base LBT plinian (IP)	VC16-48A_07	Q	5.1	28
	VC16-48B_02	Q	5.2	10
	VC16-48B_10 MI I	Q	5.0	30
	VC16-48B_10 MI II	Q	4.8	42
	VC16-48C_01	San	3.4	< dl
	VC16-48C-03	Q	4.3	32
	VC16-48C-04	Q	3.9	12
	VC16-48C-07	Q	4.9	65

followed by a slight decrease in 138 ppm at the top of the plinian pumice bed. The full data set is proved in Table 1, the ranges in concentration and standard deviations are summarised in Table 2.

Valle Toledo Member rhyolites

The VTM rhyolites are crystal-poor (< 5% crystals; Stix and Layne 1996) and typically contain fewer large, clear melt inclusions than the Bandelier pumices, especially in the early VTM deposits. We analysed 22 melt inclusions from four different VTM stratigraphic horizons: 7–3, 15–9, 15–11 and 6–8 as numbered and described by Stix (1989). These were defined by Stix (1989) and Stix and Gorton (1990a, 1990b) as representing, respectively, geochemical groups II, III, V and VI of the VTM rhyolites; for each sample we analysed, respectively, 5, 3, 6 and 8 melt inclusions. Geochemical group IV also was sampled in stratigraphic unit 6–2, and samples crushed and picked, but the few crystals present contained no melt inclusions that were large enough to analyse by FTIR.

H$_2$O concentrations in the VTM rhyolites vary between 2.0 and 4.8 wt% and are summarised in Tables 1 and 2. VTM group II is the earliest-erupted VTM material analysed here, represents residual magma after the LBT eruption (Stix and Gorton 1993) and displays H$_2$O concentrations at the lower end of the VTM range. This is followed by a slight increase in H$_2$O concentrations towards the later VTM eruptions. Looking at mean values for the geochemical groups, water contents increase 1.5 times from group II (average of 2.7 wt%) through group III (average 3.5 wt%) and group V (average 4.0 wt%), before declining to 3.0 wt% in the final VTM eruption, group VI, the age of which is within error of the UBT (Spell et al. 1996b).

The CO$_2$ evolution in the VTM rhyolites is more complex. There is a decreasing trend from the early (group II) to the late VTM (groups V and VI), but with a high-CO$_2$ excursion in group III. Average values vary from 90 ppm in group II, to 197 ppm in group III, then down to 25 ppm in both groups V and VI, for a total 3.8-fold decrease from group II to group VI and an 8.2-fold decrease from group III to group VI (Table 2).

Upper Bandelier Tuff

Crystals and melt inclusions in the UBT are very similar to those in the LBT. Melt inclusions are abundant and large (frequently up to 150–200 μm in diameter). We analysed a total of 28 melt inclusions from three different samples: the base of the UBT plinian airfall (9 melt inclusions), the top of

Table 2 Summary of the ranges and distribution of the H_2O and CO_2 concentrations per sample; SD = 1 standard deviation

Unit	H_2O (wt%)			CO_2 (ppm)		
	Range	Median	1 SD	Range	Median	1 SD
Deer Canyon Rhyolite	1.5–4.4	2.9	0.9	11–83	49	27
Top UBT plinian	2.8–4.5	3.5	0.7	37–147	90	38
Middle UBT plinian	3.1–4.3	3.7	0.4	31–137	115	36
Base UBT plinian	3.0–5.0	3.8	0.6	29–84	54	18
VTM group VI	2.0–4.2	2.9	0.7	< dl–86	16	30
VTM group V	3.0–4.8	3.9	0.6	10–46	23	12
VTM group III	3.4–3.7	(only 2 samples)		150–221	219	40
VTM group II	2.3–2.9	2.7	0.2	29–143	110	50
Top LBT plinian	2.1–5.1	4.0	0.8	63–221	140	49
Middle LBT plinian	3.2–5.2	4.3	0.7	131–223	166	31
Base LBT plinian	2.6–5.2	4.5	0.9	10–65	28	18

the plinian phase just below the transition to the ignimbrite (7 melt inclusions) and the middle of the plinian (12 melt inclusions). All three samples were collected from the same outcrop. The melt inclusions are similar in abundance and size in all three samples and no crystals nor bubbles are visible within melt inclusions.

The volatile evolution in the UBT follows a similar pattern as that in the LBT, but with smaller differences in CO_2 concentrations between the different samples. Water contents vary little within the UBT plinian (Table 2) and average water contents show minor variation and are slightly lower than those in the LBT plinian, decreasing from 3.8 wt% H_2O at the base of the plinian airfall through 3.7 wt% H_2O both in the middle and at the transition to the ignimbrite.

CO_2 follows the same trend as in the LBT, with the base of the plinian phase most depleted in CO_2 and the mid-plinian richest in CO_2 (Fig. 5, Table 2). Average CO_2 concentrations start at 54 ppm in the base, followed by a 1.9 times increase in 102 ppm in the middle and a slight decrease in 93 ppm at the top of the pumice bed.

Deer Canyon Rhyolite

The Deer Canyon Rhyolite represents the last erupted residual magma from the UBT magma chamber immediately after the UBT eruption. Crystals in the Deer Canyon Rhyolite contain many melt inclusions, but they are typically slightly smaller than in the Bandelier eruptions (mostly 80–130 μm in diameter). The glass in the inclusions is mostly colourless, but a few melt inclusions consist of darker glass. Similarly, to the Bandelier inclusions, they are free of bubbles and crystals. We analysed 10 melt inclusions from this unit.

These samples are water-poor compared to the Bandelier samples and similar to the first VTM rhyolites, with an average of 2.8 wt% H_2O. CO_2 contents are also relatively low, with concentrations between 11 and 83 ppm and an average

of 51 ppm (Table 2). From the mid-UBT plinian to the Deer Canyon Rhyolite, H_2O decreases by a factor of 1.3 and CO_2 by a factor of 1.8; for comparison with the LBT sequence, from mid-plinian LBT to VTM unit II, H_2O decreases by a factor of 1.5 and CO_2 of 1.7. These depletions in the UBT and LBT are remarkably similar.

Discussion

We now examine first the evolution in CO_2 concentrations throughout the sequence of eruptions and compare this to trends expected in a degassing magma chamber. We identify three peaks in CO_2, which can be linked to injections of fresh magma into the system. We then calculate magma storage depths based on the combined H_2O and CO_2 concentrations and determine the size of the exsolved vapour phase in both the LBT and the UBT magma chambers. Finally, we take a closer look at the excess CO_2 in the LBT to discuss the nature of the magma which was injected into the system shortly before the LBT eruption.

H₂O and CO₂ in a differentiating magma chamber

In a volatile-undersaturated melt and in the absence of crystallising phases that incorporate volatiles, H_2O and CO_2 will behave incompatibly and increase their concentrations. In contrast, in a volatile-saturated differentiating magma, both H_2O and CO_2 exsolve into a separate vapour phase. Given its lesser solubility in silicate melts, CO_2 partitions into the vapour phase more strongly than H_2O. At constant pressure and temperature as differentiation advances and volatiles exsolve from the melt, H_2O concentrations remain nearly constant, while CO_2 decreases steeply until it is exhausted in the melt (Wallace et al. 1995, 1999; Lowenstern 2001; Blundy et al. 2010). In the case of the Bishop Tuff, a large

silicic magma body with a number of similarities to the Bandelier Tuff, Wallace et al. (1995, 1999) found that H_2O contents and incompatible elements decreased from the top down into the magma chamber, while CO_2 concentrations increased.

To establish whether a melt was volatile-saturated before eruption, we examine the contrasting behaviour of H_2O, CO_2, F and Cl. Fluorine is a highly incompatible trace element which is similar in behaviour to Cs, accumulating in the melt whether it is volatile-saturated or not (Stix and Layne 1996). Other volatiles, such as H_2O, CO_2 and Cl are incompatible only under volatile-undersaturated conditions and partition into a vapour phase as soon as one is present. The contrasting accumulation trends of these different volatile species can, therefore, indicate whether a silicate melt is volatile-saturated. Various studies point towards volatile saturation in the Bandelier magma chamber. Hervig and Dunbar (1992) established the LBT ignimbrite was erupted from a volatile-saturated melt, based on contrasting H_2O and F behaviour. Stix and Layne (1996) argued a vapour phase was present during the VTM, based on the different accumulation patterns of H_2O, fluorine and chlorine. Waelkens et al. (2021) showed strong fractionation between F and Cl throughout the LBT–VTM–UBT sequence; both F and Cl are enriched in the earliest erupted materials (plinian airfall phases) compared to the end of the LBT and UBT sequences (respectively earliest VTM and Deer Canyon Rhyolite), but the fluorine enrichment is substantially greater than that of chlorine. This fractionation between F and Cl hence demonstrates that the entire sequence was volatile-saturated and a vapour phase was present (Fig. 6).

Our sampling strategy allows us to look at three main trends within the Bandelier sequence: (1) the LBT magma chamber as primed for eruption, preserved in the sequence from the base of the plinian (first-erupted material) to VTM group II (last-erupted material from the LBT magmatic system); (2) the evolution of the top of the magma chamber during its re-establishment and evolution between the two Bandelier eruptions, from VTM group III to VTM group VI; (3) the pre-eruptive UBT magma chamber, preserved in the sequence from the base of the plinian airfall (first-erupted material) to the Deer Canyon Rhyolite (last-erupted material in the UBT sequence).

The recent studies on residence times of melt in a magma chamber and on magma chamber structure have altered the once dominant model of a magma chamber that exists as a large, mostly liquid reservoir for long periods of time (e.g. Bachmann and Bergantz 2004, 2008; Gualda and Ghiorso 2013). Estimated near-solidus temperatures of 660–725 °C for the magma in the Bandelier magma chamber before eruption imply the magma was highly crystalline (Campbell et al. 2009; Wilcock et al. 2013) and fit a scenario of an extensive magma mush

which was remelted shortly before eruption. Yet while the Bandelier Tuff is unlikely to have erupted from a single large mostly liquid magma chamber that was systematically tapped and is more likely to have been formed through progressive remelting of a crystal mush due to repeated magma intrusions (cf. Wolff and Ramos 2014), or from a more complex configuration than a single chamber, we argue that it is reasonable to consider the LBT and UBT sequences as compositionally continuous sequences, with the first erupted material the most evolved and the last erupted material the least evolved. For example, measured fluorine concentrations in melt inclusions of the LBT–VTM–UBT sequence (Fig. 6) show that F, which behaves as an incompatible element in the Bandelier sequence (Stix and Layne 1996), is most enriched to very high concentrations reaching ~ 3000 ppm in the plinian airfall of both the LBT and UBT and is strongly depleted in the last-erupted materials (respectively the earliest VTM and the Deer Canyon Rhyolite). This pattern is consistently shown by other strongly incompatible trace elements, such as Cs and Nb (e.g. Stix and Gorton 1993).

Lower Bandelier Tuff

Measured concentrations of F and Cl in melt inclusions from the same stratigraphic horizon (data from Waelkens et al. 2021; Fig. 6) show higher concentrations of incompatible fluorine at the base of the airfall unit and a progressive decrease in fluorine towards the end of the LBT sequence. Cl follows a similar, but less pronounced pattern, since Cl was progressively removed from the melt and partitioned into a separate vapour phase, with the first-erupted LBT airfall material having undergone the largest degree of degassing. Based on these halogen concentrations and on observed H_2O–CO_2 patterns in the Bishop Tuff (Wallace et al. 1995, 1999), we expect the base of the LBT plinian to have very low CO_2 with increasing concentrations at deeper levels in the magma chamber, while H_2O should vary little. Mean observed H_2O contents vary slightly through the plinian LBT (4.0–4.2 wt%), decreasing to some degree in VTM group II (mean of 2.7 wt%), which could be linked to different storage depths (see Gas saturation pressures). However, the CO_2 pattern is unexpected. CO_2 concentrations are very low at the base of the LBT, as we would expect in the roof zone of the magma chamber where the magma is most differentiated and most degassed. However, instead of a progressive increase towards the later erupted material, a sharp increase in higher CO_2 concentrations occurs halfway through the plinian phase (from a mean of 27 ppm at the base of the plinian airfall to 173 ppm in the mid-plinian), followed by a decrease to an apparently bimodal CO_2 distribution in the first-erupted VTM. This unexpected increase in CO_2 implies an additional, external source of CO_2.

Valle Toledo Member rhyolites

The VTM sequence represents an evolving magma related to the Bandelier Tuff that was episodically tapped between the two Bandelier eruptions (Stix and Gorton 1993; Stix and Layne 1996). As the melt was volatile-saturated (Stix and Layne 1996), we expect H_2O to vary little, as it is buffered by the vapour phase, while CO_2 should decrease steadily as the magma was differentiated and CO_2 exsolved to the vapour phase. H_2O concentrations do indeed vary little; the slightly lower water contents of VTM groups II and VI may result from different storage depths (see Gas saturation pressures below), while groups III and V have similar water concentrations (respective averages of 3.5 and 3.9 wt% H_2O). Group VI, the most evolved and degassed of the VTM magmas is the most depleted in CO_2 as expected. The highest average CO_2 in the entire LBT-VTM-UBT sequence is found in group III (mean of 197 ppm), followed by a steep decrease in very low concentrations in groups V and VI. The anomalously high CO_2 of group III again points towards an external addition of CO_2 into the differentiating magma chamber.

Upper Bandelier Tuff

The observed volatile patterns in the UBT sequence are similar to the LBT, although less pronounced. The base of the plinian phase has similar water content as the LBT and slightly higher CO_2 (means of 27 ppm in LBT, 54 ppm in UBT). This higher CO_2 content suggests that the UBT magma was less degassed than in the LBT, consistent with higher Cl concentrations and higher F/Cl ratios in the UBT (Fig. 6; Waelkens et al. 2021). The CO_2 enrichment from the base of the plinian airfall to mid-plinian is less pronounced than in the LBT, yet also present, indicating similar processes in both cases.

Influx of CO_2 into the magma chamber

Throughout the LBT-VTM-UBT sequence, therefore, we have three clear instances of "excess" CO_2, where CO_2 concentrations are higher than expected: (1) the LBT mid-plinian; (2) VTM group III; and (3) the UBT mid-plinian. We propose that these high CO_2 concentrations are caused by the interaction of the Bandelier magma with CO_2-rich vapours, which exsolved from fresh, volatile-saturated magma that was injected into the magma chamber shortly before the Bandelier eruptions and during the early VTM, after which the CO_2-rich vapours percolated upwards through the crystal mush. This process, often described as CO_2 fluxing or flushing, has been recognised and modelled in arc magmas (Wallace 2005; Spilliaert et al. 2006; Collins et al. 2009; Blundy et al. 2010; Caricchi et al. 2018) and has also been

suggested in large silicic magma bodies, such as the Bishop Tuff (Evans et al. 2016), even though these are usually assumed to follow simple open or closed degassing trends (Blundy et al. 2010).

CO_2 injections into the magma chamber linked to magma recharge

A number of lines of evidence point towards repeated intrusions of fresh magma into the Bandelier magma chamber before, during and after the caldera-forming eruptions took place. Based on the trace element composition of LBT melt inclusions, Dunbar and Hervig (1992) and Hervig and Dunbar (1992) suggested that repeated pulses of rhyolite magma were intruded into the base of the LBT magma chamber shortly before eruption, while Wolff and Ramos (2014) using Sr and Pb isotopic data found evidence of at least three separate magma recharge events into a crystal mush which generated melting of the mush and possibly triggered the LBT eruption. A Ti-in-quartz geothermometry study of the LBT and VTM by Campbell et al. (2009) found evidence of injection of a hotter magma into the chamber shortly before the eruption. Stix and Gorton (1993) showed that an influx of fresh rhyolitic magma occurred once the chamber was partially emptied by the LBT eruption; this influx occurred between the eruption of VTM groups II and III. Stimac (1996) proposed that the hornblende-dacite pumices observed in early-erupted UBT resulted from injection of intermediate magma into the UBT magma chamber shortly before the eruption. Wilcock et al. (2013) found further evidence of hot magma interacting with the deeper parts of the UBT magma chamber before eruption. In the upper UBT ignimbrite, Goff et al. (2014) found evidence of andesitic magma injection into the chamber during the eruption. Kennedy et al. (2012) discussed the influx of dacitic magma into the emptied UBT magma chamber during post-collapse resurgence.

We propose that these injections of magma were accompanied by exsolution of CO_2-rich gases, which were added to the magma system prior to eruptions. As modelled by Caricchi et al. (2018), when CO_2 is added to a CO_2-poor, volatile-saturated magma at constant confining pressure, CO_2 is transferred from the vapour phase into the magma, while H_2O is exsolved from the magma. The addition of CO_2 leads to a reduction of the activity of H_2O, in turn increasing the solidus and liquidus temperatures, which then triggers crystallisation (Holloway and Burnham 1972). This new onset of crystallisation will form crystals that contain melt inclusions enriched in CO_2 relative to those prior to magma injection.

First CO_2 injection: Lower Bandelier Tuff

The injection of a CO_2-rich vapour phase into the magmatic system allows us to explain the patterns we observe in the Lower Bandelier Tuff. Based on the Ti geothermometry in quartz, Campbell et al. (2009) concluded the LBT magma chamber was at near-solidus temperatures, until it was revived by reheating from injection of hot magma into the system shortly before eruption. Pre-eruptive heating events in crystal mushes are common; while they are linked to the influx of fresh magma, the most efficient way to transport heat from one magma to the other is through upward migration of a hot vapour phase, rather than through hybridization or conductive heating (Bachmann and Bergantz 2006). This implies that the fresh magma introduced into the system was itself volatile-saturated and exsolved a CO_2-rich vapour phase which percolated through the magma chamber and rejuvenated the near-solidus magma.

Without the influx of this additional CO_2 into the magmatic system, we would expect the LBT magma to have followed the 'expected' pattern of a degassed magma: the lowest CO_2 concentrations at the most-degassed first-erupted material and an increase in CO_2 upward in the stratigraphy, paired with a decrease in H_2O. Given the very low CO_2 concentrations at the base of the LBT plinian, typical of a very degassed magma, we propose that the base of the plinian airfall represents the pristine degassed Bandelier magma, free from interference with percolated CO_2. Although we need to be careful when interpreting the CO_2 concentrations of VTM group II as truly bimodal given that only five melt inclusions were analysed, the apparent occurrence of both CO_2-poorer melt inclusions (29–45 ppm) and CO_2-richer inclusions (110–143 ppm) (Fig. 7) may be interpreted as representing both (1) a degassed, "original" melt that predates the CO_2 influx (CO_2-poor inclusions) and (2) a CO_2-rich melt resulting from CO_2 fluxing (CO_2-rich inclusions). The "original" volatile profile, if no CO_2 fluxing had occurred, is therefore one with means of 4.2 wt% H_2O and 27 ppm CO_2 at the top of the chamber and means of 2.7 wt% H_2O and 37 ppm CO_2 at its base. The H_2O gradient was strong, while the CO_2 gradient was weak.

Before eruption, fresh magma entered the magma chamber, accompanied by a vapour phase comparatively rich in CO_2. The fresh magma increased the temperature at the base of the magma chamber, melting the mush and allowing gas to percolate upward through the mush. Following this short period of transient remelting, temperatures decreased again, triggering crystallisation and encapsulating CO_2-rich melt inclusions into newly-formed crystals which are preserved in the upper parts of the LBT plinian. We propose that the CO_2-rich melt inclusions above the base of the plinian phase are the product of interaction with the vapour phase that percolated upward from the injected magma; they do not represent the actual hotter and newly injected magma. The injected magma itself only interacted with material at the base of the crystal mush, traces of which have been found in the ignimbrite (Ti–rich melt inclusions: Dunbar and Hervig 1992; Sr- and Ba-rich overgrowth on Sr- and Ba-poor cores in sanidines: Wolff and Ramos 2014).

The lack of high temperature rims on quartz crystals from the plinian airfall observed by Campbell et al. (2009) and the lack of high-CO_2 melt inclusions at the base of the plinian airfall observed by us, together indicate that CO_2 fluxing was not spread equally throughout the system and the CO_2-rich vapours did not reach the top of the chamber.

Second CO_2 injection: Valle Toledo Member rhyolites

In contrast to the LBT and UBT sequences which allow us to see a snapshot through time of the pre-eruptive magmatic system before eruption, the VTM sequence provides us a window into the temporal evolution of the magma chamber's upper regions. The first-erupted VTM material, group II, is the last remnant of the LBT magma, containing material both from the 'old' resident magma and from the injected magma (Stix and Layne 1996), which explains its apparent bimodal CO_2 concentrations. Stix and Gorton (1993) recognised the next eruptive VTM phase, group III, as the beginning of a new evolutionary trend after fresh magma had entered the magma chamber following caldera collapse. Campbell et al. (2009) found quartz crystals in this unit to be unzoned and formed at slightly lower temperatures than group II crystals. The high CO_2 concentrations measured in VTM group III are consistent with these observations. Fresh, CO_2-rich magma entered the emptied magmatic system, started crystallising and formed CO_2-rich melt inclusions, which were then erupted. Further evolution of this new magma throughout the VTM led to decreasing CO_2 concentrations as CO_2 was fractionated from the volatile-saturated melt into the vapour phase, similarly to Cl (Fig. 6). H_2O changed little as degassing took place, buffered by the composition of the vapour phase and stable pressure configuration of the magmatic system.

This trend is interrupted in VTM group VI, where H_2O decreases from a mean of 4.0 wt% to 3.0 wt% H_2O. This decrease was not observed by Stix and Layne (1996), where H_2O concentrations were found to change little in the upper VTM. The lower volatile content of this final VTM magma may result from a shallower storage depth than the rest of the magma chamber (see Gas saturation pressures below).

Within the lower VTM (groups II–III), the range of H_2O values appear to be restricted, although H_2O concentrations were obtained for only two melt inclusions in group III. The upper VTM (groups V–VI) exhibits wider ranges of H_2O (i.e., 1.8 wt% variation for V and 2.2 wt% variation for VI),

while the range in CO_2 values for group VI is also relatively large (below detection limit to 88 ppm). This larger range in CO_2 concentrations and increase in higher CO_2 values in group VI could indicate that CO_2 fluxing was being initiated and hot CO_2-rich vapour bubbles were being injected into the magma chamber even before the UBT eruption. Quartz geothermometry confirms this, with a very small fraction of crystals in group VI exhibiting high temperature overgrowths (Campbell et al. 2009). Crystals from different stages of VTM magma evolution also could explain some of the variation in H_2O and CO_2. Most of the variation in H_2O concentrations in groups V and VI may be due to crystals formed at different depths being erupted at the same time, indicating the final VTM eruptions were tapping different levels in the upper parts of the magma chamber.

Third CO_2 injection: Upper Bandelier Tuff

An influx of CO_2-rich vapours that percolated through a crystal mush can also explain the observed volatile enrichments in the UBT. However, a few key differences are discernible relative to the LBT: (1) the lowest CO_2 concentrations at the base of the UBT plinian airfall unit are higher than at the base of the LBT plinian; (2) traces of foreign magma (dacite) appear in the plinian phase and early erupted ignimbrite (Stimac 1996); (3) the increase in CO_2 from the base to mid-plinian is smaller; (4) there is overlap in CO_2 contents between the base and the mid-plinian airfall; (5) the end of the UBT sequence (Deer Canyon Rhyolite) is more complex than seen at the end of the LBT (VTM group II). Relative to the LBT plinian base, the higher CO_2 values at the base of the UBT plinian may be partly the result of less degassing prior to eruption, evidence of which can also be found in the higher Cl concentrations in the UBT compared to the LBT (Fig. 6). However, the UBT plinian is not only richer in CO_2 than the LBT plinian, it is also richer than the uppermost VTM (unit VI). Hence the high CO_2 observed in the initial stages of the UBT eruption cannot simply be the result of continued differentiation and degassing of the magma tapped by the VTM eruptions; it must have experienced a different means of CO_2 enrichment.

This early CO_2 enrichment of the UBT is significant. Although in the LBT major and trace element evidence of the intruded magma can only be recognised in the later stages of eruption, the UBT erupted a small proportion of distinctive dacitic pumices beginning in the early stages of the plinian phase. This dacite is not cogenetic with the Bandelier magmas and is the result of injection of a dacite into the rhyolite crystal mush before eruption (Stimac 1996; Boro et al. 2020). Further evidence of magma injections is preserved in zoned crystals in the upper parts of the ignimbrite, while rounded quartz crystal morphologies indicate

widespread resorption throughout the magma chamber (Wilcock et al. 2013).

For the UBT sequence, an increase in CO_2 and slight decrease in H_2O are observed through the plinian airfall, suggestive of a scenario similar to the LBT with an initially degassed, CO_2-poor magma. Fresh magma was injected and a CO_2-rich vapour percolated upward through a crystal mush, increasing the CO_2 content of the melt and triggering crystallisation of crystals encapsulating CO_2-rich melt inclusions. Injection of CO_2 into the magmatic system must have occurred in order to explain the high CO_2 values in the plinian phase, which are nearly twice those of the Deer Canyon Rhyolite that erupted immediately after the UBT. Otherwise, CO_2 concentrations would increase with decreasing degree of differentiation from the base of the plinian airfall (first-erupted, most differentiated material in the UBT sequence) to the Deer Canyon Rhyolite (last-erupted, least differentiated material erupted in the UBT sequence), which is not observed.

A significant point is that Wilcock et al. (2013) did not observe zoned or high temperature crystals in the plinian phase and early erupted ignimbrite (units 1 and 2 of Warren et al. 2007). If CO_2-rich vapour percolated through the magma chamber, transporting heat and volatiles and enriching the melt in CO_2, the CO_2-rich melt inclusions should be formed within distinctive high temperature overgrowths on crystals, yet no such overgrowths were recognised by Wilcock et al. (2013). Hence, we suggest that CO_2-rich vapours were introduced into the magma chamber as small batches of fresh magma accumulated at the base of the magma chamber (or deeper) over a prolonged period of time before eruption, starting in the late VTM; thereby, gradually increasing the CO_2 content of the magma chamber without substantial rapid increases in temperature. Smith (1979) proposed the presence of a deeper basaltic zone of magma underlying the Bandelier magma chamber. Pooling of basaltic magma at depth would release CO_2-rich gases that could rise to more shallow depths; thereby, interacting with the Bandelier magma (cf. Collins et al. 2009).

As the magma was crystallising and differentiating and CO_2 levels slowly increased from the late VTM onwards, progressively more CO_2-rich melt inclusions were encapsulated. In contrast to the steep increase in CO_2 prior to the LBT eruption, the more gradual increase in CO_2 in the UBT magma chamber explains the wide range of CO_2 concentrations, the enrichment in CO_2 compared to the VTM and the less systematic CO_2 increase over the course of the plinian phase of the eruption. Although influx of dacitic magma, accompanied by an increase in temperature may have triggered the eruption (Stimac 1996; Wilcock et al. 2013; Boro et al. 2020), CO_2-rich vapours from intruded magma had been adding CO_2 to the magmatic system since the late VTM, prior to the dacite intrusive event. The gradual

system-wide increase in CO_2 for the UBT explains the smaller increase in CO_2 from the base to the mid- and top of the plinian airfall, in contrast to the sudden change observed at a comparable point in the LBT eruption.

The Deer Canyon Rhyolite does contain zoned crystals with high temperature rims and is interpreted as a product of hotter new magma remelting a residual crystal mush of composition similar to the late-erupted UBT (Kennedy et al. 2012; Wilcock et al. 2013). CO_2 concentrations in the Deer Canyon Rhyoite are not bimodally distributed as they appear to be in VTM group II immediately after the LBT eruption, while the base of the UBT plinian has elevated CO_2 concentrations in some melt inclusions as discussed above. Thus, it is more difficult to reconstruct the 'original' volatile profile that would have been displayed in the UBT volcanic products if no CO_2 fluxing had taken place. Our best approximation is 3.7 wt% H_2O in the first-erupted, most differentiated material (base of the plinian airfall) and 1.9 wt% H_2O in the last-erupted, least differentiated material (Deer Canyon Rhyolite). Because of the relatively high CO_2 seen throughout the plinian airfall, we are unable to develop a similar profile for CO_2.

Variability in H_2O concentrations

Throughout the LBT-VTM-UBT sequence, all analysed samples display a wide range of H_2O contents, particularly in the LBT and the Deer Canyon Rhyolite. A number of processes could contribute to this variability. (1) Melt inclusions formed at different depths may have been erupted together, having been transported to different levels of the magma chamber by convective currents. (2) Some of the melt inclusions could have suffered H_2O loss due to diffusion through the crystal. While quartz is usually considered an excellent host for melt inclusions and less likely to experience post-entrapment changes in melt inclusions compared to other minerals (Audétat and Lowenstern 2014), heating experiments on quartz-hosted melt inclusions from the Bishop Tuff found that water loss started to occur if the melt inclusions were heated at 800 °C for more than 12 h (Severs et al. 2007). The influx of heat into the system during the magmatic recharge events may have sufficiently heated some crystals to cause H_2O loss, particularly if there was a H_2O gradient between the entrapped melt inclusion and the surrounding magma. (3) Substantial pre-eruptive degassing of H_2O and CO_2 took place in the system and melt inclusions were trapped at different stages of the degassing process. Closed-system degassing trends for the different stages of the LBT plinian airfall (Fig. 8a) demonstrate that degassing of elevated H_2O–CO_2 starting compositions could have produced some of the variability in volatile concentrations, in particular for the base of the plinian. The calculated closed-system degassing trend for the Deer Canyon Rhyolite

(Fig. 8d) indicates that this process was dominant in creating the large range of H_2O concentrations for this unit. The degassing trends are less clear in the UBT plinian airfall and VTM units. Nevertheless, a combination of pre-eruptive degassing and a limited degree of H_2O loss due to heating and diffusion could also explain the trends that we observe in these sequences as well.

Alternative sources of CO_2

The influx and percolation of CO_2 through a crystal mush prior to eruption can explain the patterns we observe in CO_2 concentrations throughout the LBT–VTM–UBT sequence. This model is consistent with previously established magmatic recharge events in the Bandelier system. Nevertheless, we must also consider other possible sources of the "excess" CO_2 in the system. Carbonates are an alternative external source of CO_2 that are recognised to play an important role in certain CO_2-rich volcanic systems, such as Somma-Vesuvius (e.g. Dallai et al. 2011) and Merapi (e.g. Deegan et al. 2010). Although bulk assimilation of carbonates by a melt can lead to high dissolved CO_2 concentrations in the melt, such an assimilation process should be recognisable in the trace element geochemistry of the melt. Using $^{18}O/^{16}O$ rations and chemical data at Vesuvius, Dallai et al. (2011) were able to identify CO_2 which originated from a deeper carbonate basement and entered the magmatic system. However, the crustal basement under Valles caldera shows no evidence of extensive carbonates and oxygen isotope studies of the Bandelier Tuff (Wolff et al. 2002) have not identified the strongly sedimentary $^{18}O/^{16}O$ signals that the influx of carbonate-derived CO_2 should generate. Hence, we believe it unlikely that carbonates played an important role in producing the CO_2 influxes which entered the Bandelier magmatic system.

Gas saturation pressures

We have shown above that the entire LBT–VTM–UBT magma system was gas-saturated, based on various lines of evidence. Hence, we can use H_2O and CO_2 concentrations to calculate saturation pressures of the magma (Fig. 8; Table A3 in Supplementary Information). Only melt inclusions with highest water are considered, given that lower H_2O values may be due to H_2O loss after reheating. Using VolatileCalc (Newman and Lowenstern 2002), we calculate saturation pressures of 124–168 MPa for the LBT plinian and 100–143 MPa for the UBT plinian for a magma temperature of 700 °C (temperature estimate from Campbell et al. 2009 and Wilcock et al. 2013). As these pressures are calculated from the first-erupted plinian phases, they indicate the pressure in the uppermost parts of the magma chamber. Assuming a crustal density of 2700 kg m^{-3} (Stix

and Layne 1996), we calculate depths of 4.7–6.3 km for the top of the LBT magma chamber and 3.8–5.4 km for the UBT magma chamber. These depths are at the lower end of previous estimates, which have placed both the LBT and the UBT magmas between 5 and 7 km (Sommer 1977; Warshaw and Smith 1988; Dunbar and Hervig 1992; Stix and Layne 1996; Wilcock et al. 2013; Goff et al. 2014). The shallower depth of the UBT magma chamber could be the result of modified magmatic plumbing due to caldera collapse during the LBT eruption. For example, the LBT eruption and associated caldera collapse may have opened a network of fractures, which allowed subsequent UBT magma to ascend to shallower levels and might also have facilitated the eruption of the VTM rhyolites.

A similar calculation for the VTM leads to pressures of 38–60 MPa in group II, 80–101 MPa in III, 103–123 MPa in V and 71–93 MPa in VI. This results in very shallow crystallisation depths for groups II (1.4–2.2 km) and VI (2.7–3.5 km), with greater depths for III (3.0–3.8 km) and V (3.9–4.6 km). The Deer Canyon Rhyolite pressures are 66–113 MPa and a depth of 2.5–4.3 km. The shallow depth of group II VTM magma likely relates to its timing immediately after the LBT eruption, when the system was still open and depressurised after caldera collapse. The shallow depths of group VI VTM magma could indicate that a small batch of magma managed to separate from the main magma chamber and intrude to shallower levels. Importantly, there is no unconformity or time gap in the stratigraphic record between group VI VTM and the UBT plinian. Hence the eruption of this shallow VTM magma could have initiated events leading to the subsequent UBT super-eruption.

## Nature and volume of the exsolved vapour phase

Exsolved vapour phase

As fluorine behaves incompatibly in the melt similar to elements, such as Cs (Stix and Layne 1996), we can use the enrichment of F to estimate how much H_2O and CO_2 were exsolved to the vapour phase. In the absence of mineral phases that incorporate volatiles, H_2O and CO_2 will be enriched similar to F in a volatile-undersaturated melt. Any deviation from this enrichment trend is due to the melt being volatile-saturated and H_2O and CO_2 partitioning into the vapour phase. By calculating the difference between the theoretical enrichment of H_2O and CO_2 and the measured enrichment or depletion, we can estimate the mass of volatiles that was lost to the vapour phase. The clear distinction between CO_2-poor and CO_2-enriched melt compositions in the LBT is ideal for this exercise. This approach is more complicated for the UBT, where the difference between the original, degassed melt and the post-injection CO_2-rich melt is less obvious.

We first consider the degassed, CO_2-poor melt inclusions at the base of the LBT plinian airfall (most differentiated, first-erupted material) and in the low-CO_2 melt inclusions of VTM group II (least differentiated, last-erupted material). The mid-plinian and group II VTM CO_2-rich melt inclusions are considered to represent the magma chamber after CO_2 enrichment due to gas percolation associated with magma recharge. Although the magma chamber is unlikely to have existed as a single, large entity and, as discussed above, a more complicated geometry with a crystal mush component that underwent repeated remelting is likely, for this calculation and for simplicity, we consider the entire erupted LBT magma as a single, cylindrical body with surface area equal to the preserved caldera area (i.e., a circular caldera with diameter of 20 km) and volume equal to that which was erupted (550 km^3; maximum estimate from Cook et al. 2016). This configuration allows us to calculate CO_2 masses through a simple integration of the CO_2 gradient through the cylindrical volume of the magma chamber.

Fluorine is enriched by 6.6 times between VTM group II and the base of the LBT plinian (Waelkens et al. 2021; see Fig. 6). A similar enrichment in CO_2, starting from a CO_2 concentration of 37 ppm at or near the base of the simplified, cylindrical magma chamber (mean of CO_2-poor concentrations in VTM group II) would result in a concentration of 243 ppm at the top of the chamber. Integrating this theoretical concentration gradient over the entire mass of the cylindrical magma chamber results in a total mass of 181 Tg CO_2. Meanwhile, integrating the observed concentration gradient (37 ppm near the base of the chamber to a mean of 27 ppm in the base of the LBT plinian) results in a total mass of CO_2 present in the melt phase of 41 Tg. A total of 140 Tg of CO_2 is therefore 'missing' and must have partitioned into a vapour phase. A similar exercise can be done for H_2O, starting from a concentration of 2.6 wt% in VTM group II. A theoretical 6.6-fold enrichment results in an unrealistically high H_2O concentration of 17 wt% and a total H_2O mass of 1.27×10^5 Tg, while the observed enrichment, from 2.6 wt% near the base of the magma chamber to 4.2 wt% at the top results in a mass of 4.37×10^4 Tg H_2O. A mass of 8.3×10^4 Tg H_2O was therefore lost to the vapour phase. In a magma chamber of 550 km^3 volume (assuming the magma chamber was largely emptied during eruption) and 2275 kg/m^3 density (calculated based on the composition of Hervig and Dunbar 1992), these masses of exsolved H_2O and CO_2 result in a vapour phase that represents 6.7 wt% of the total magma body. This estimate is slightly higher than calculations by Wallace et al. (1995) for the Bishop Tuff magma body (2–6 wt%).

A similar calculation can be done for the UBT, where fluorine is enriched 4.4 times from the Deer Canyon Rhyolite (base of the magma chamber) to the base of the UBT
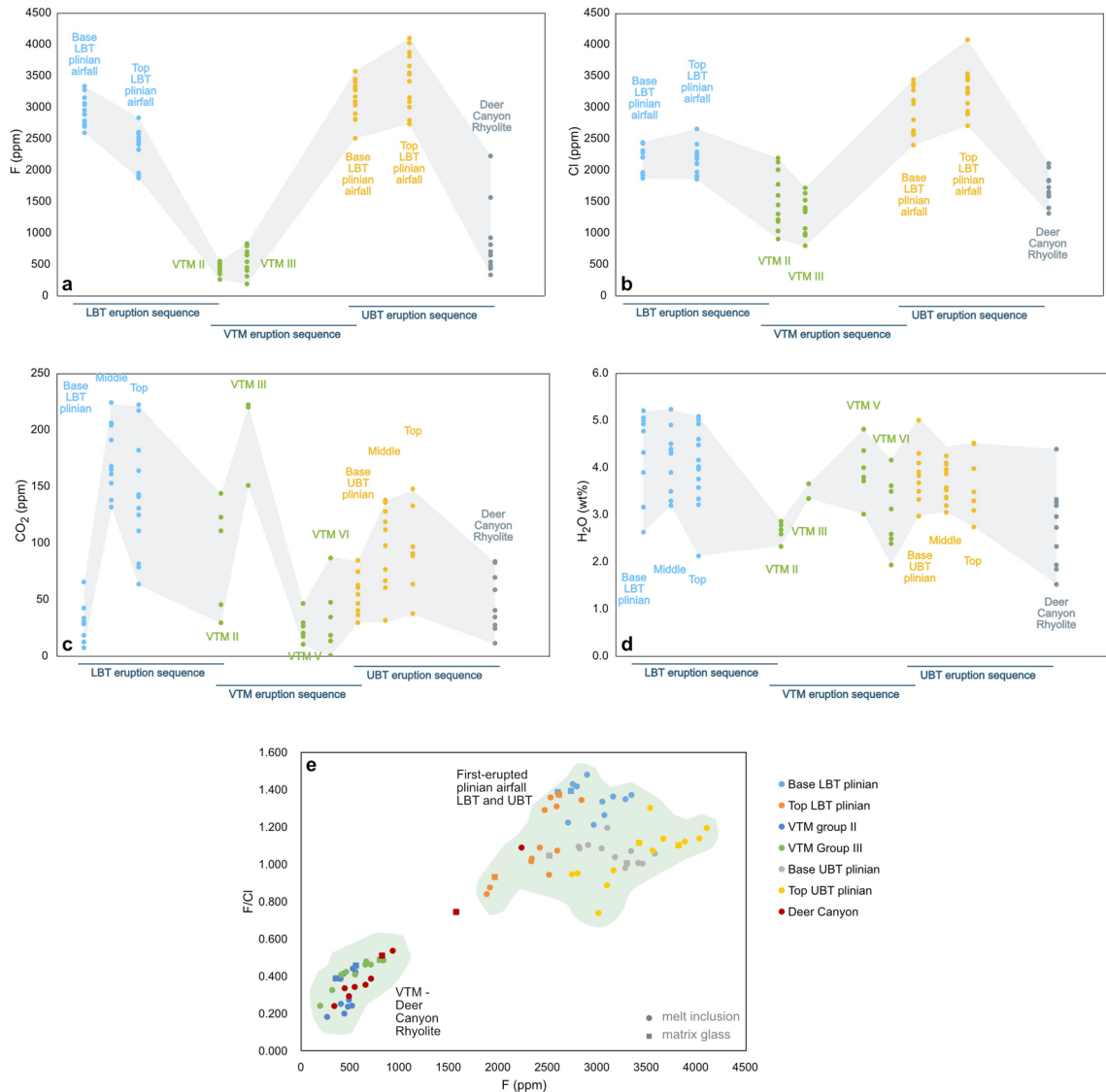
Fig. 6 Plots of **a** F, **b** Cl, **c** CO_2 and **d** H_2O data along the stratigraphy. The F and Cl data was collected by SIMS on different melt inclusions from the exact same samples as the FTIR data presented here. **e** F/Cl ratios give an indication of the degree of degassing that the magma experienced: as F behaves as an incompatible element in this magmatic system while Cl partitions into a vapour phase, F/Cl ratios increase with advancing degassing

plinian (top of the chamber) (Waelkens et al. 2021). The measured mean composition for the Deer Canyon Rhyolite is 2.8 wt% H_2O and 51 ppm CO_2, while mean values at the base of the plinian phase are 3.8 wt% H_2O and 54 ppm CO_2. Using an estimated magma chamber volume of 400 km^3 (estimated erupted volume from Goff et al. 2014, 2011) and assuming the magma chamber was largely emptied during eruption, results in 78 Tg CO_2 and 3.86×10^4 Tg H_2O lost from the magma. Comparing this to the mass of magma, with density of 2281 kg/m^3, calculated from

compositions in Stix and Layne (1996), results in a vapour phase that is 4.2 wt% of the total magma body.

Waelkens et al. (2021) calculated the masses of chlorine partitioned from the magma body into a separate fluid phase for both the LBT and the UBT, similarly as we did here for H_2O and CO_2. A mass of 4.8×10^3 Tg of Cl was calculated to have been exsolved in the LBT magma chamber and 2.1×10^3 Tg in the UBT. Combining this with the exsolved water masses calculated above results in weight fractions of chlorine in the fluid of 5.8 wt% in the LBT

Fig. 7 Histograms of CO_2 concentrations for all analysed units, using bin widths of 25 ppm CO_2. The samples are ordered per stratigraphic unit: Lower Bandelier Tuff (LBT) plinian in the first column, Valle Toledo Member (VTM) rhyolites in the second and Upper Bandelier Tuff (UBT) plinian in the third. In each column, the samples are presented according to stratigraphic position. The sharp increase in CO_2 concentrations from the base to the middle of the LBT plinian is clear in the histograms, with CO_2 concentrations spread over a wider range in the top of the LBT plinian. In contrast, CO_2 concentrations overlap more between the base and the middle of the UBT plinian, although ranges in CO_2 concentrations are once again larger in the middle and top of the plinian
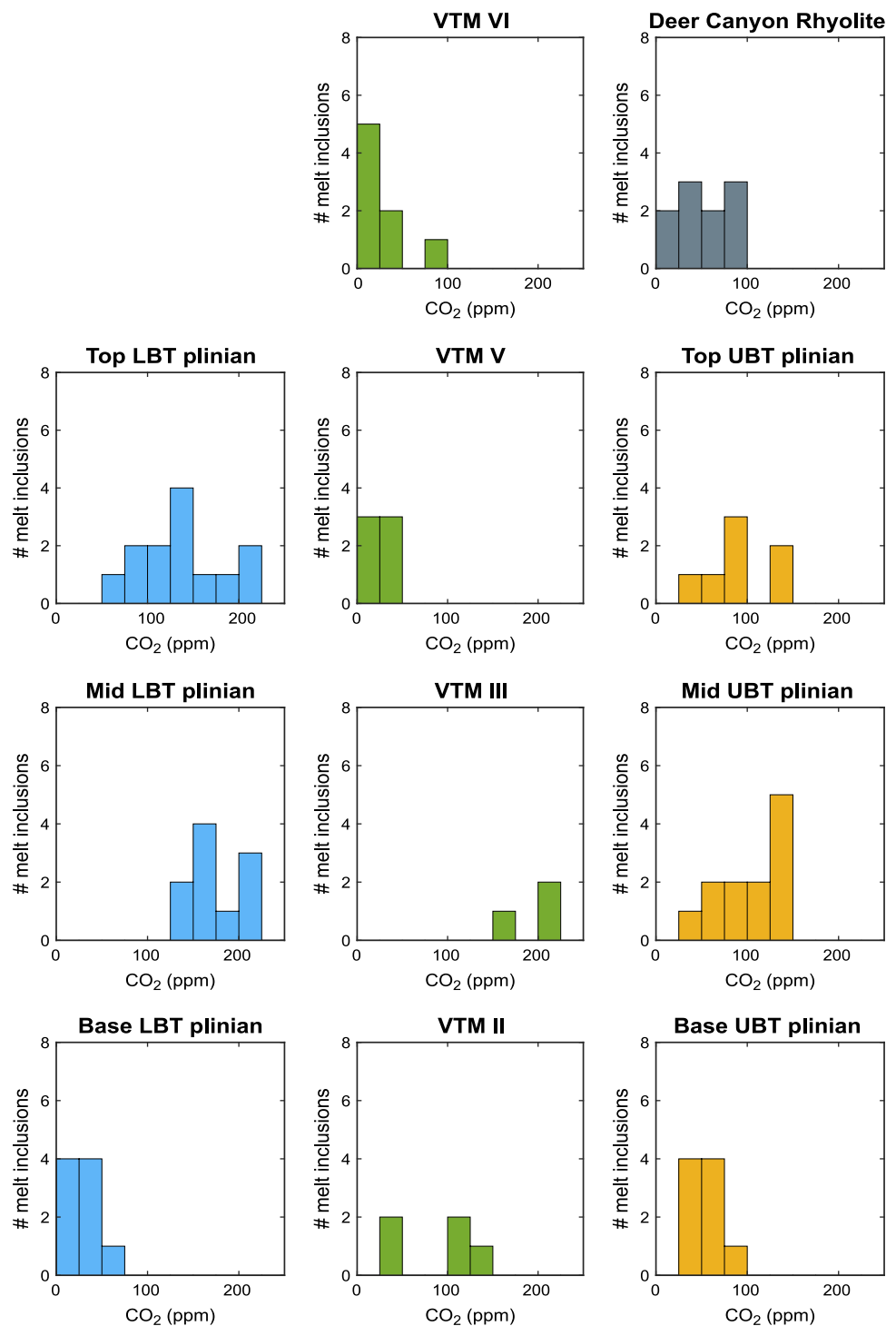
and 5.4 wt% in the UBT. Recalculated to NaCl we obtain respectively 9.6 and 8.9 wt% NaCl for the LBT and the UBT. Based on the phase equilibria in the NaCl-H_2O-CO_2 system (Duan et al. 1995), at a temperature of 700 °C and a pressure range of 100–150 MPa, the exsolved phase would exist as two immiscible phases: a brine rich in NaCl and a separate H_2O–CO_2 vapour.

In these calculations, we assume that the entire exsolved vapour was preserved and accumulated in the magmatic system prior to the large caldera-forming eruptions although there is evidence that exsolved vapours can accumulate at the top of a differentiating magma chamber from where they are released upon eruption (eg. Westrich and Gerlach 1992; Gerlach et al. 1994), some of the vapour

Fig. 8 H_2O and CO_2 concentrations for **a** the LBT plinian; **b** the VTM rhyolites; **c** the UBT plinian; and **d** the Deer Canyon Rhyolite. Isobars are plotted for 700 °C and were determined using VolatileCalc (Newman and Lowenstern 2002). The stark contrast in CO_2 concentrations between the base of the LBT plinian airfall and the rest of the plinian phase is clearly illustrated, as is the smaller increase in CO_2 upsection in the UBT plinian. The VTM groups II and VI plot at lower pressures than the rest of the VTM, while VTM group III exhibits the highest CO_2 values of the entire dataset. Closed-system degassing trends and H_2O loss explain part of the intrasample variability in H_2O concentrations, while entrapment at different stages of the CO_2 fluxing process can explain part of the variability in CO_2 concentrations within samples
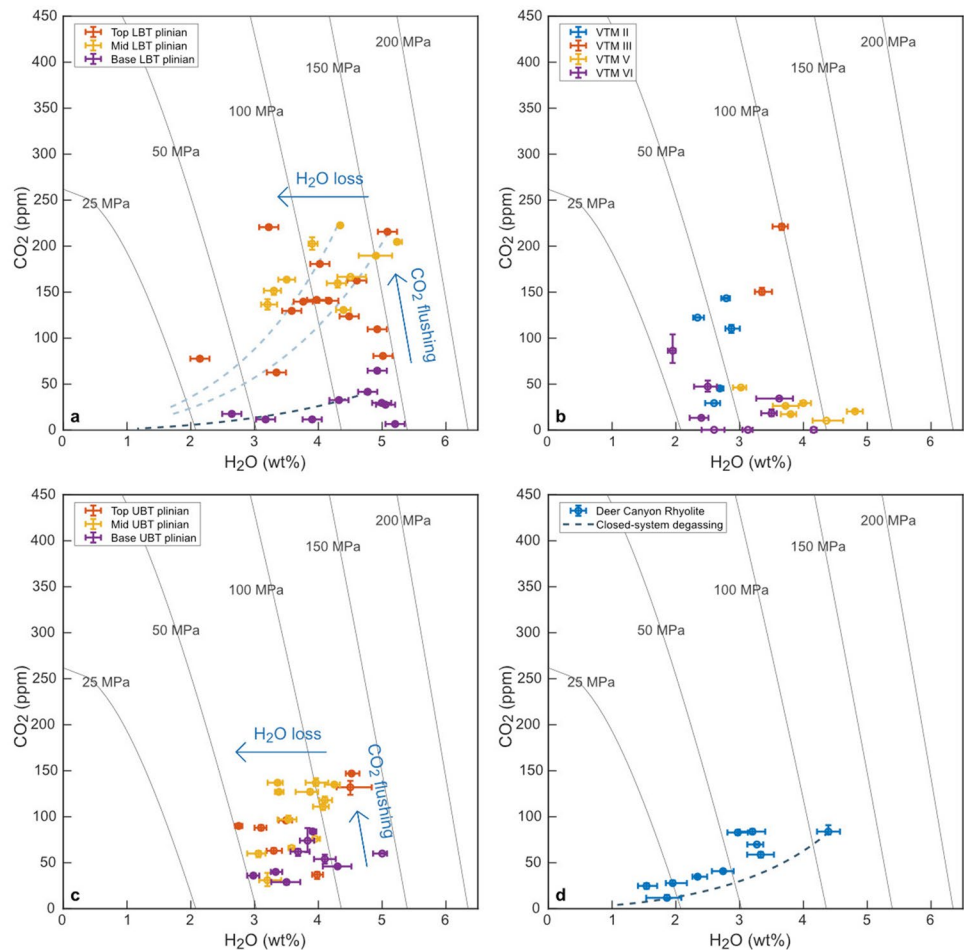
could have escaped the magmatic system before the eruption. The calculated vapour phase volumes should therefore be considered maxima.

Nature of influx magma

Using the same reasoning as above, we now calculate the mass of CO_2 that was injected into the degassed LBT magma chamber by comparing the CO_2-poor, degassed trend (CO_2-poor melt inclusions of VTM group II and the base of the plinian phase) to the CO_2-rich, post-injection trend (CO_2-rich melt inclusions of VTM group II and mid-plinian). We only do this exercise for the LBT, as the trends of low and high CO_2 are clearly distinguishable here. Although we do see CO_2 enrichment in the UBT that can be explained by magma recharge, the pre-injection and post-injection CO_2 groups cannot be easily distinguished from each other compared to the LBT. We calculate that increasing the dissolved CO_2 content of the magma chamber from 37 ppm CO_2 at the bottom of the chamber and 27 ppm CO_2 at the top to 125 ppm at the bottom and 173 ppm at the top requires an input of 150 Tg of CO_2. Such an input carried

by a rhyolitic magma containing 200 ppm CO_2 requires a volume of 329 km³, which is excessive. This indicates that the magma injected into the chamber was different in composition from the resident magma, as suggested by Dunbar and Hervig (1992). The magma is more likely to have been more basaltic, as basaltic magmas typically have higher CO_2 content (Lowenstern, 2001), so that smaller volumes of magma would need to be injected and degas to bring an extra 150 Tg of CO_2 into the magma chamber. A basalt with CO_2 concentration of 500 ppm carries 150 Tg of CO_2 in 103 km³ magma; for a basalt with 1000 ppm CO_2, this volume goes down to 52 km³.

Conclusions

Our principal conclusions are the following:

1. By examining the evolution of CO_2 concentrations through the different stages of the Bandelier magmatic system, we identified three instances of "excess" CO_2, where higher CO_2 concentrations were measured than

would be expected: the middle of the LBT plinian phase, VTM group III and the middle of the UBT plinian phase. We link these peaks in CO_2 concentrations to influxes of volatile-saturated, fresh magma into the system, whereby CO_2-rich vapours exsolved from the injected magma percolated through the magmatic system and interacted with the melt.

2. In the LBT magmatic system we distinguish two trends: (1) the CO_2-poor, degassed magma, preserved at the base of the LBT plinian (first-erupted, most differentiated material) and the low-CO_2 VTM group II melt inclusions (last-erupted, least differentiated LBT material) and (2) the CO_2-rich magma resulting from fresh CO_2 vapours that percolated through the magmatic system; this CO_2-rich component is preserved in the LBT mid-plinian and the CO_2-rich melt inclusions also found in VTM group II. The large range of CO_2 concentrations in the LBT plinian unit implies a rapid succession of separate recharge events; thereby, supporting earlier studies on the LBT.

3. CO_2 concentrations in the VTM rhyolites record replenishment of the magma chamber after the LBT eruption (VMT group III), followed by degassing of the differentiating magma.

4. Similar to the LBT, the UBT plinian airfall shows evidence of increased CO_2 concentrations due to injections of CO_2-rich vapour from fresh magma, but the smaller contrast and generally higher CO_2 concentrations than in the LBT indicate a more gradual CO_2 enrichment. The presence of CO_2-rich melt inclusions in VTM group VI indicate that the percolation of CO_2-rich vapour in the magmatic system had already begun in late VTM time.

5. By comparing theoretical and observed enrichments in H_2O and CO_2, we calculate that in the LBT magmatic system exsolved a vapour phase representing a maximum of 6.7 wt% of the total magma body. A similar calculation for the UBT results in a maximum vapour phase of 4.2 wt%.

6. Our results indicate that volatile compositions of large silicic magmatic systems can record instances of magmatic recharge. CO_2, thereby, is an important tool in deciphering the recharge events that feed these large eruptions.

Declarations

References

Audétat A, Lowenstern JB (2014) Melt inclusions. In: Turekian K, Holland H (eds) Treatise on geochemistry, 2nd edn. Elsevier, pp 143–173

Bachmann O, Bergantz GW (2004) On the origin of crystal-poor rhyolites: extracted from batholithic crystal mushes. J Petrol 45:1565–1582

Bachmann O, Bergantz GW (2006) Gas percolation in upper-crustal silicic crystal mushes as a mechanism for upward heat advection and rejuvenation of near-solidus magma bodies. J Volcanol Geoth Res 149:85–102

Bachmann O, Bergantz GW (2008) Rhyolites and their source mushes across tectonic settings. J Petrol 49:2277–2285

Balsley SD (1988) The petrology and geochemistry of the Tshirege Member of the Bandelier Tuff, Jemez Mountains volcanic field, New Mexico, U.S.A. MSc thesis, University of Texas at Arlington

Behrens H, Tamic N, Holtz F (2004) Determination of the molar absorptions coefficient for the infrared absorption band of CO_2 in rhyolitic glasses. Am Miner 89:301–306

Blundy J, Cashman KV, Rust A, Witham F (2010) A case for CO_2-rich arc magmas. Earth Planet Sci Lett 290:289–301

Boro JR, Wolff JA, Neill OK (2020) Anatomy of a recharge magma: Hornblende dacite pumice from the rhyolitic Tshirege Member of the Bandelier Tuff, Valles Caldera, New Mexico, USA. Contrib Miner Petrol 175:1–26

Broxton DE, Heiken GH, Chipera SJ, Byers FM Jr (1995) Stratigraphy, petrography, and mineralogy of Bandelier Tuff and Cerro Toledo deposits. Earth Sci Invest Environ Restoration 21:33–65

Brundstad KA (2013) Origin and evolution of large silicic caldera complex: Valles caldera and the associated Upper Bandelier Tuff. PhD thesis, Washington State University

Campbell ME, Hanson JB, Minarik WG, Stix J (2009) Thermal history of the Bandelier magmatic system: evidence for magmatic injection and recharge at 1.61 Ma as revealed by cathodoluminescence and titanium geothermometry. J Geol 117:469–485

Caress ME (1996). Zonation of alkali feldspar compositions in the Tshirege Member of the Bandelier Tuff in Pueblo Canyon, near Los Alamos, New Mexico. In: Goff F, Kues BS, Roger MA, McFadden LS & Gardner JN (eds) Jemez Mountains Region. New Mexico Geological Society 47th Annual Fall Field Conference Guidebook, pp 275–283

Caricchi L, Sheldrake TE, Blundy J (2018) Modulation of magmatic processes by CO_2 flushing. Earth Planet Sci Lett 491:160–171

Collins SJ, Pyle DM, Maclennan J (2009) Melt inclusions track pre-eruption storage and dehydration of magmas at Etna. Geology 37:571–574

Cook GW, Wolff JA, Self S (2016) Estimating the eruptive volume of a large pyroclastic body: the Otowi member of the Bandelier Tuff, Valles caldera, New Mexico. Bull Volcanol 78:10. https://doi.org/10.1007/s00445-016-1000-0

Dallai L, Cioni R, Boschi C, D'Oriano C (2011) Carbonate-derived CO_2 purging magma at depth: Influence on the eruptive activity of Somma-Vesuvius, Italy. Earth Planet Sci Lett 310:84–95

Deegan FM, Troll VR, Freda C, Misiti V, Chadwick JP, McLeod CL, Davidson JP (2010) Magma-carbonate interaction processes and associated CO_2 release at Merapi volcano, Indonesia: Insights from experimental petrology. J Petrol 51:1027–1051

Devine JD, Gardner JE, Brack HP, Layne GD, Rutherford MJ (1995) Comparison of microanalytical methods for estimating H_2O contents of silicic volcanic glasses. Am Miner 80:319–328

Duan Z, Møller N, Weare JH (1995) Equation of state for the $NaCl-H_2O-CO_2$ system: prediction of phase equilibria and volumetric properties. Geochim Cosmochim Acta 59:2869–2882

Dunbar NW, Hervig RL (1992) Volatile and trace element composition of melt inclusions from the Lower Bandelier Tuff: implications for magma chamber processes and eruptive style. J Geophys Res 97:151–170

Eichelberger JC, Koch FG (1979) Lithic fragments in the Bandelier Tuff, Jemez Mountains, New Mexico. J Volcanol Geoth Res 5:115–134

Evans BW, Hildreth W, Bachmann O, Scaillet B (2016) In defense of magnetite-ilmenite thermometry in the Bishop Tuff and its implication for gradients in silicic magma reservoirs. Am Miner 101:469–482

Gardner JN, Goff F, Kelley S, Jacobs E (2010) Rhyolites and associated deposits of the Valles-Toledo caldera complex. New Mex Geol 32:3–18

Gerlach TM, Westrich HR, Casadevall TJ, Finnegan DL (1994) Vapor saturation and accumulation in magmas of the 1989–1990 eruption of redoubt Volcano, Alaska. J Volcanol Geoth Res 62:317–337

Goff F (2010) The Valles caldera: new Mexico's supervolcano. New Mexico Earth Matters 10:1–4

Goff F, Gardner JN (2004) Late Cenozoic geochronology of volcanism and mineralization in the Jemez Mountains and Valles caldera, north central New Mexico. In: Mack GH, Giles KA (eds) The geology of New Mexico: a geologic history. New Mexico Geological Society Special Publication, pp 295–311

Goff F, Gardner JN, Baldridge WS, Hulen JB, Nielson DL, Vaniman D, Heiken G, Dungan MA, Broxton D (1989) Excursion 17B: Volcanic and hydrothermal evolution of Valles caldera and Jemez volcanic field. N Mex Bur Mines Miner Resource Mem 46:381–434

Goff F, Warren RG, Goff CJ, Dunbar N (2014) Eruption of reverse-zoned upper Tshirege Member, Bandelier Tuff from centralized vents within Valles caldera, New Mexico. J Volcanol Geoth Res 276:82–104

Goff F, Gardner JN, Reneau SL, Kelley SA, Kempter KA, Lawrence JR (2011) Geologic map of the Valles caldera, Jemez Mountains, New Mexico. New Mexico Bureau of Geology and Mineral Resources, Geologic Map 79, scale 1:50,000

Griggs RL (1964) Geology and groundwater resources of the Los Alamos area New Mexico. Geological Survey Water-supply paper 1753. U.S. Government Printing Office, Washington, DC. https://doi.org/10.3133/wsp1753

Gualda GAR, Ghiorso MS (2013) The Bishop Tuff giant magma body: an alternative to the Standard Model. Contrib Miner Petrol 166:755–775

Heiken G, Goff F, Stix J, Tamanyu S, Shafiqullah M, Garcia S, Hagan R (1986) Intracaldera volcanic activity, Toledo Caldera and Embayment, Jemez Mountains, New Mexico. J Geophys Res 91:1799–1815

Hervig RL, Dunbar NW (1992) Cause of chemical zoning in the Bishop (California) and Bandelier (New Mexico) magma chambers. Earth Planet Sci Lett 111:97–108

Holloway JR, Burnham CW (1972) Melting relations of basalt with equilibrium water pressure less than total pressure. J Petrol 13:1–29

Jacobs EP, Kelley SA (2007) The time between the tuffs: deposits of the Cerro Toledo interval in Bandelier National Monument, New Mexico. In: Kues BS, Kelley SA, Lueth VW (eds) Geology of the Jemez Region II. New Mexico Geological Society 58th Annual Fall Field Conference Guidebook, pp 308–315

Kennedy B, Wilcock J, Stix J (2012) Caldera resurgence during magma replenishment and rejuvenation at Valles and Lake City calderas. Bull Volcanol 74:1833–1847

Kuentz DC (1986) The Otowi Member of the Bandelier Tuff: A study of the petrology, petrography, and geochemistry of an explosive silicic eruption, Jemez Mountains, New Mexico. MSc thesis, University of Texas at Arlington

Lowenstern JB (2001) Carbon dioxide in magmas and implications for hydrothermal systems. Miner Deposita 36:490–502

Lucic G, Berg A-S, Stix J (2016) Water-rich and volatile-undersaturated magmas at Hekla volcano, Iceland. Geochem Geophys Geosyst 17:3111–3130

Luhr JF (2001) Glass inclusions and melt volatile contents at Parícutin volcano, Mexico. Contrib Miner Petrol 142:261–283

Newman S, Lowenstern JB (2002) Volatile calc: a silicate melt–H_2O–CO_2 solution model written in visual basic for excel. Comput Geosci 28:597–604

Newman S, Stolper EM, Epstein S (1986) Measurement of water in rhyolitic glasses-calibration of an infrared spectroscopic technique. Am Miner 71:1527–1541

Newman S, Epstein S, Stolper E (1988) Water, carbon dioxide, and hydrogen isotopes in glasses from the ca. 1340 A.D. eruption of the Mono Craters, California: constraints on degassing phenomena and initial volatile content. J Volcanol Geoth Res 35:75–96

Nielson DL, Hulen JB (1984) Internal geology and evolution of the Redondo dome, Valles caldera, New Mexico. J Geophys Res 89:8695–8711

Phillips EH, Goff F, Kyle PR, McIntosh WC, Dunbar NW, Gardner JN (2007) The $^{40}Ar/^{39}Ar$ age constraints on the duration of resurgence at the Valles caldera, New Mexico. J Geophys Res. https://doi.org/10.1029/2006JB004511

Rowe MC, Wolff JA, Gardner JN, Ramos FC, Teasdale R, Heikoop CE (2007) Development of a continental volcanic field: petrogenesis of pre-caldera intermediate and silicic rocks and origin of the Bandelier magmas, Jemez Mountains (New Mexico, USA). J Petrol 48:2063–2091

Self S, Goff F, Gardner JN, Wright JV, Kite WM (1986) Explosive rhyolitic volcanism in the Jemez Mountains: vent locations, caldera development and relation to regional structure (USA). J Geophys Res 91:1779–1798

Severs MJ, Azbej T, Thomas JB, Mandeville CW, Bodnar RJ (2007) Experimental determination of H_2O loss from melt inclusions during laboratory heating: evidence from Raman spectroscopy. Chem Geol 237:358–371

Slate JL, Sarna-Wojicki AM, Wan E, Dethier DP, Wahl DB, Lavine A (2007) A Chronostratigraphic Reference Set of Tephra Layers From the Jemez Mountains Volcanic Source, New Mexico. In: Kues BS, Kelley SA, Lueth VW (eds) Geology of the Jemez Region II. New Mexico Geological Society 58th Annual Fall Field Conference Guidebook, pp 239–247

Smith RL (1979) Ash-flow magmatism. Geol Soc Am Spec Pap 180:5–27

Smith RL, Bailey RA (1968) Resurgent cauldrons. In: Coats RR, Hay RL, Anderson CA (eds) Studies in volcanology, vol 116. Geological Society of America Memoirs, pp 613–662

Smith RL, Bailey RA, Ross CS (1970) Geologic map of the Jemez Mountains, New Mexico. U.S. Geologic Survey, map I-571, scale 1:125,000. https://doi.org/10.3133/i571

Sommer MA (1977) Volatiles H_2O, CO_2 and CO in silicate melt inclusions in quartz phenocrysts from the rhyolitic Bandelier air-fall and ash-flow tuff, New Mexico. J Geol 85:423–432

Spell TL, Harrison TM, Wolff JA (1990) $^{40}Ar/^{39}Ar$ dating of the Bandelier Tuff and San Diego Canyon ignimbrites, Jemez Mountains, New Mexico: temporal constraints on magmatic evolution. J Volcanol Geoth Res 43:175–193

Spell TL, McDougall I, Doulgeris AP (1996b) Cerro Toledo Rhyolite, Jemez Volcanic Field, New Mexico: $^{40}Ar/^{39}Ar$ geochronology of eruptions between two caldera-forming events. Bull Geol Soc Am 108:1549–1566

Spell TL, Kyle PR, Baker J (1996a). Geochronology and geochemistry of the Cerro Toledo Rhyolite. In: Goff F, Kues BS, Roger MA, McFadden LS, Gardner JN (eds) Jemez Mountains Region. New Mexico Geological Society 47th Annual Fall Field Conference Guidebook, pp 263–268

Spilliaert N, Allard P, Métrich N, Sobolev AV (2006) Melt inclusion record of the conditions of ascent, degassing, and extrusion of volatile-rich alkali basalt during the powerful 2002 flank eruption of Mount Etna (Italy). J Geophys Res. https://doi.org/10.1029/2005JB003934

Stimac JA (1996) Hornblende-dacite pumice in the Tshirege Member of the Bandelier Tuff: Implications for magma chamber and eruptive processes. In: Goff F, Kues BS, Roger MA, McFadden LS, Gardner JN (eds) Jemez Mountains Region. New Mexico Geological Society 47th Annual Fall Field Conference Guidebook, pp 269–274

Stix J, Gorton MP (1990a) Changes in silicic melt structure between the two Bandelier caldera-forming eruptions, New Mexico, USA: evidence from zirconium and light rare earth elements. J Petrol 31:1261–1283

Stix J, Gorton MP (1990b) Variations in trace element partition coefficients in sanidine in the Cerro Toledo Rhyolite, Jemez Mountains, New Mexico: effects of composition, temperature, and volatiles. Geochim Cosmochim Acta 54:2697–2708

Stix J, Gorton MP (1993) Replenishment and crystallization in epicontinental silicic magma chambers: evidence from the Bandelier magmatic system. J Volcanol Geoth Res 55:201–215

Stix J, Layne GD (1996) Gas saturation and evolution of volatile and light lithophile elements in the Bandelier magma chamber between two caldera-forming eruptions. J Geophys Res 101:25181–25196

Stix J, Goff F, Gorton MP, Heiken G, Garcia SR (1988) Restoration of compositional zonation in the Bandelier silicic magma chamber between two caldera-forming eruptions: geochemistry and origin of the Cerro Toledo Rhyolite, Jemez Mountains, New Mexico. J Geophys Res 93:6129–6147

Stix J (1989) Physical and chemical fractionation processes in subaerial and subaqueous pyroclastic rocks. PhD thesis, University of Toronto

Turbeville BN, Self S (1988) San Diego canyon ignimbrites: pre-Bandelier tuff explosive rhyolitic volcanism in the Jemez mountains, New Mexico. J Geophys Res 93:6148–6156

Waelkens CM, Stix J, Monteleone B, Burckel P (2021) Efficient release of bromine by super-eruptions. Geology 49:1416–1420. https://doi.org/10.1130/G49114.1

Wallace PJ (2005) Volatiles in subduction zone magmas: Concentrations and fluxes based on melt inclusion and volcanic gas data. J Volcanol Geoth Res 140:217–240

Wallace PJ, Anderson ATJ, Davis AM (1995) Quantification of pre-eruptive exsolved gas contents in silicic magmas. Nature 377:612–616

Wallace PJ, Anderson AT Jr, Davis AM (1999) Gradients in H_2O, CO_2, and exsolved gas in a large-volume silicic magma system: Interpreting the record preserved in melt inclusions from the Bishop Tuff. J Geophys Res 104:20097–20122

Warren RG, Goff F, Kluk EC, Budahn JR (2007). Petrography, chemistry, and mineral compositions for subunits of the Tshirege Member, Bandelier Tuff within the Valles Caldera and Pajarito Plateau. In: Kues BS, Kelley SA, Lueth VW (eds) Geology of the Jemez Region II. New Mexico Geological Society 58th Annual Fall Field Conference Guidebook, pp 316–332

Warshaw CM, Smith RL (1988) Pyroxenes and fayalites in the Bandelier Tuff, New Mexico: temperatures and comparison with other rhyolites. Am Miner 73:1025–1037

Westrich HR, Gerlach TM (1992) Magmatic gas source for the stratospheric SO_2 cloud from the June 15 1991, eruption of Mount Pinatubo. Geology 20:867–870

Wilcock J, Goff F, Minarik WG, Stix J (2013) Magmatic recharge during the formation and resurgence of the Valles caldera, New Mexico, USA: evidence from quartz compositional zoning and geothermometry. J Petrol 54:635–664

Wilcock J (2010) Magmatic Recharge during the Formation and Resurgence of the Valles Caldera, New Mexico, USA: Evidence from Quartz Compositional Zoning and Geothermometry. MSc thesis, McGill University

Wolff JA, Gardner JN (1995) Is the Valles caldera entering a new cycle of activity? Geology 23:411–414

Wolff JA, Ramos FC (2014) Processes in caldera-forming high-silica rhyolite magma: Rb-Sr and Pb isotope systematics of the Otowi member of the Bandelier Tuff, Valles Caldera, New Mexico, USA. J Petrol 55:345–375

Wolff JA, Balsley SD, Gregory RT (2002) Oxygen isotope disequilibrium between quartz and sanidine from the Bandelier Tuff, New Mexico, consistent with a short residence time of phenocrysts in rhyolitic magma. J Volcanol Geoth Res 116:119–135

Wolff JA, Ellis BS, Ramos FC, Starkel WA, Boroughs S, Olin PH, Bachmann O (2015) Remelting of cumulates as a process for producing chemical zoning in silicic tuffs: a comparison of cool, wet and hot, dry rhyolitic magma systems. Lithos 236–237:275–286

Zhang Y, Belcher R, Ihinger PD, Wang L, Xu Z, Newman S (1997) New calibration of infrared measurement of dissolved water in rhyolitic glasses. Geochim Cosmochim Acta 61:3089–3100